Using Optical Tweezers, Single Molecule Fluorescence and the ZIF268 Protein-DNA System to Probe Mechanotransduction Mechanisms

by

Peter Lee
B.A.Sc. Engineering Science
University of Toronto, 2001

Submitted to the Biological Engineering Division in
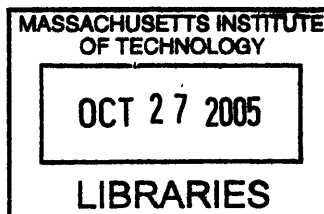Partial Fulfillment of the Requirements for the Degree of

Master of Science in Bioengineering
at the
Massachusetts Institute of Technology
[February 2006]
July 2005

Signature of Author ....

Biological Engineering Division
July 15, 2005

Certified by ....
Matthew J. Lang
Assistant Professor
Biological Engineering Division
Department of Mechanical Engineering

Accepted by ....
Alan J. Grodzinsky
Professor
Biological Engineering Division
Department of Electrical Engineering and Computer Science
Department of Mechanical Engineering
Chairman, Committee for Graduate Students

.

Using Optical Tweezers, Single Molecule Fluorescence and the ZIF268 Protein-DNA System to Probe Mechanotransduction Mechanisms

by

Peter Lee

Optical tweezers instruments use laser radiation pressure to trap microscopic dielectric beads. With the appropriate chemistry, such a bead can be attached to a single molecule as a handle, permitting the application of force on the single molecule. Measuring the force applied in real-time is dependent on detecting the bead's displacement from the trapping laser beam axis. Back-focal-plane detection provides a way of measuring the displacement, in two-dimensions, at nanometer or better resolution. The first part of this work will describe the design of a simple and inexpensive position sensing module customized for optical tweezers applications.

Single molecule fluorescence is another powerful technique used to obtain microscopic details in biological systems. This technique can detect the arrival of a single molecule into a small volume of space or detect the conformational changes of a single molecule. Combining optical tweezers with single-molecule fluorescence so that one can apply forces on a single molecule while monitoring its effects via single molecule fluorescence provides an even more powerful experimental platform to perform such microscopic studies. Due to the enhanced photobleaching of fluorophores caused by the trapping laser, this combined technology has only been demonstrated under optimized conditions. The second part of this work will describe a straightforward and noninvasive method of eliminating this problem.

The study of mechanotransduction in biological systems is critical to understanding the coupling between mechanical forces and biochemical reactions. Due to the recent advances in single molecule technology, it is now possible to probe such mechanisms at the single molecule level. The third and final part of this work will describe a basic mechanotransduction experiment using the well-studied ZIF268 protein-DNA system. An experimental assay and method of analysis will be outlined.

Table of Contents

List of Figures

List of Tables

Chapter 1: Back-focal-plane displacement detection

Optical tweezers is one of the powerful techniques used in single-molecule biophysics research. It permits the application of known forces on single molecules. A single-beam gradient force optical trap, first demonstrated by Ashkin et al. in 1986 (reference 1), can trap micron-sized dielectric beads. Because forces can be applied to these beads, attachment of a bead to a single molecule enables one to apply forces on single molecules in solution, as illustrated schematically in Figure 1.
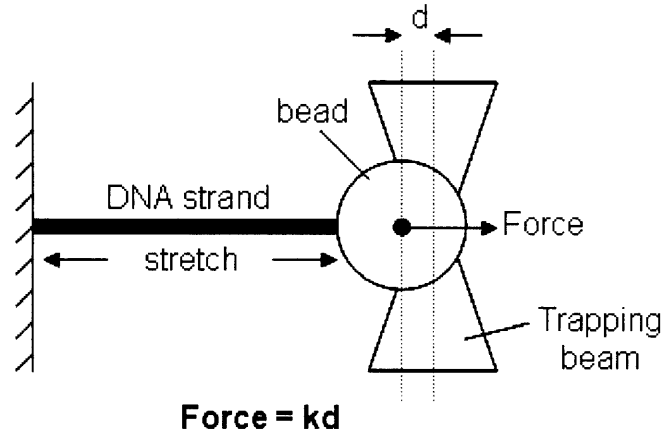
Figure 1. Sample experiment demonstrating the power of optical tweezers. Here, a known force is applied along the DNA strand.

Because theoretically calculating the applied forces is currently difficult and unreliable, modern optical tweezers use a different approach for measuring forces. The optical trap can be approximated as a harmonic potential and, hence, one can imagine the bead as being attached to a Hookean spring. As shown in Figure 1, if the bead is displaced a distance d from the center of a trap with a spring constant k, the applied force on the bead, and consequently the molecule it is attached to, is equal to kd. Therefore, detecting the displacement of the bead is equivalent to measuring the applied force, once the spring constant is known. In addition, measuring the spring constant also relies on being able to measure the bead's displacement. Various methods of measuring the spring constant k can be found in references 2 and 3.

Back-focal-plane displacement detection is a method of measuring the two-dimensional bead displacement. The theory underlying this technique is outlined in reference 4. The basic principle behind this method is illustrated in Figure 2. Consider a detection laser beam that is aligned and collinear with the trapping laser beam. Both beams pass through the objective collimated. The size of the detection beam's waist at the focal plane is roughly ~500nm. As can be seen in Figure 2, part of the detection beam light gets scattered by the dielectric bead. An intensity pattern is formed in the far-field due to the interference of the scattered and unscattered light. Because the scattering is altered as the bead displaces from the central beam axis, so does the intensity pattern. In fact, this two-dimensional intensity pattern can be projected onto the active area of a position sensing photodiode, thereby permitting the measurement of bead displacements.
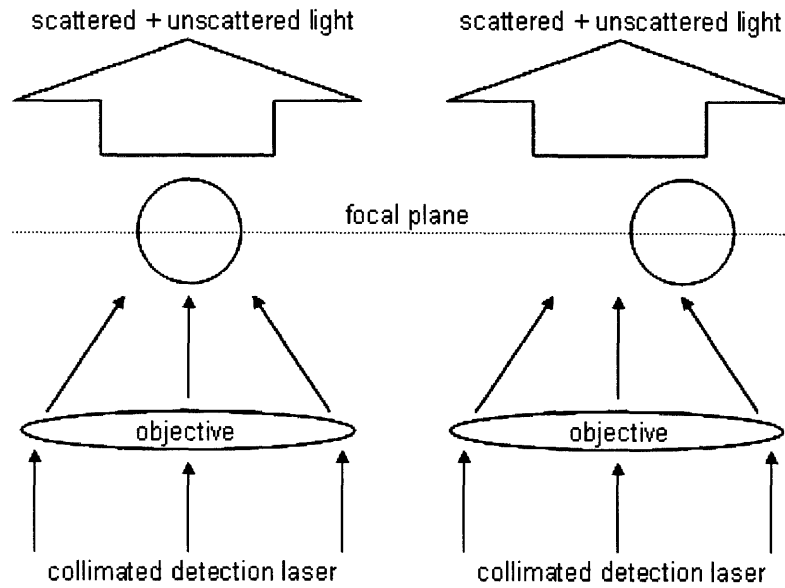
Figure 2. The basic principle behind back-focal-plane displacement detection.

The intensity pattern resulting from the scattered and unscattered light is located in the back-focal-plane of the condenser. By using the optical layout shown in Figure 3, this image can be projected onto a position sensing photodiode. The filter is needed to filter out light from the trapping laser. Since the typical trapping and detection laser wavelengths are 1064nm and 975nm, respectively, a low pass filter will suffice. The dichroic mirror is needed to reflect near infrared (IR) light while transmitting visible light from the microscope lamp.
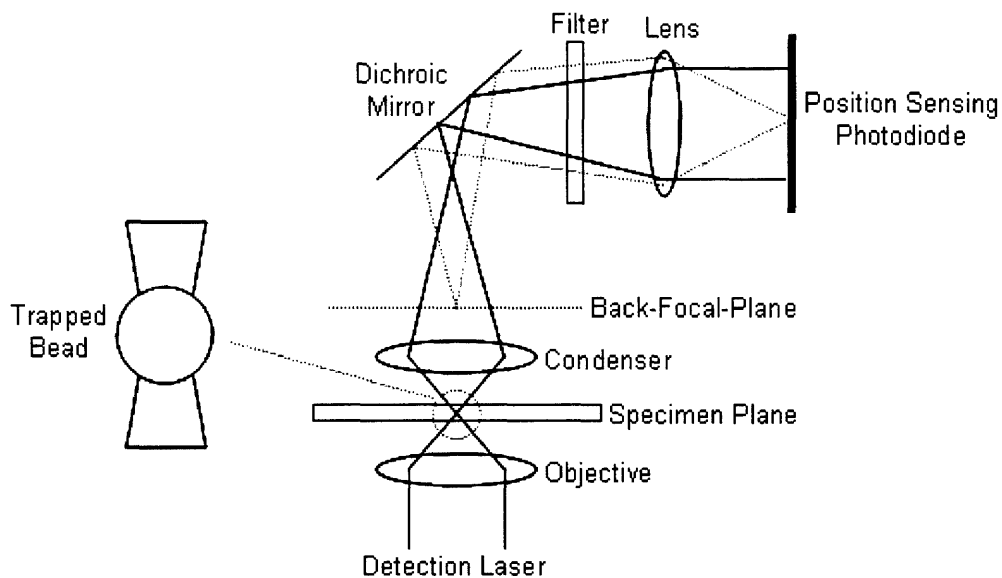
Figure 3. Schematic diagram of displacement detection branch in an optical tweezers instrument.

As mentioned above, the intensity pattern changes as the bead is displaced. More importantly, the centroid of intensity changes. Since two-dimensional position sensing photodiodes are designed to measure the location of the intensity centroid in its active area, it represents the perfect optical sensor solution to the problem of bead displacement

12

detection. An example of such a sensor integrated with signal processing circuits is shown in Figure 4.
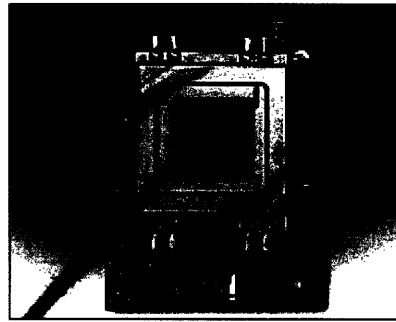
Figure 4. Position sensing module (DL100-7PCBA, Pacific Silicon Sensor Inc.).

The reason for having both a trapping and detection beam is for calibration purposes. In an actual experiment, both beams will always be aligned so that if the bead is pulled away from its equilibrium position, it will be displaced from the common central axis of both beams. But having separate control of the trapping beam allows one to move the bead a known displacement from the detection beam. The power of the detection beam must be at least two-orders of magnitude lower than that of the trapping beam as to apply negligible force on the bead itself. Since the image projected onto the position sensing photodiode is formed from the detection beam, a relationship between known displacements and the image intensity centroid can be established. If one views the projected image with an IR viewer while the bead is swept through the detection beam, a moving 'blob' can be seen as shown in Figure 5.
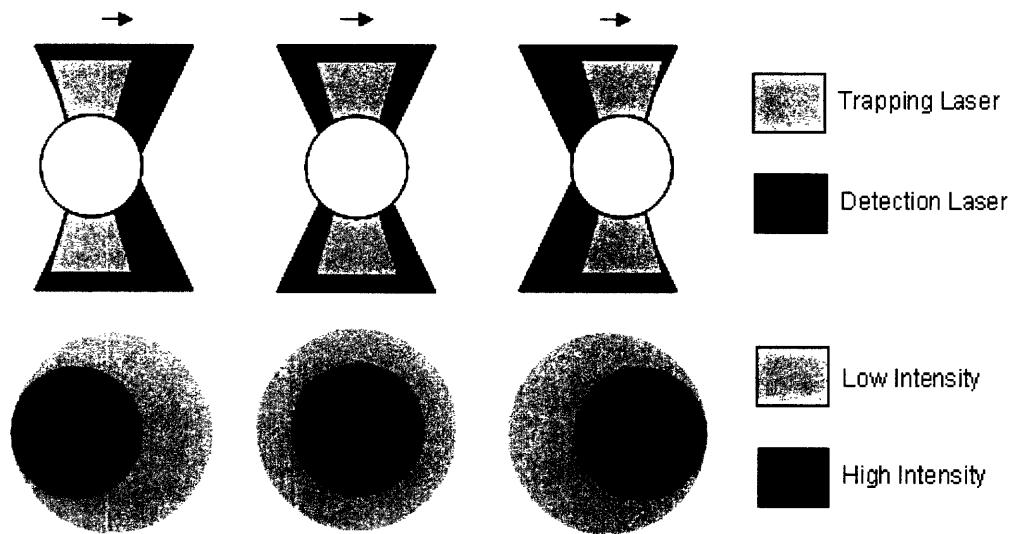
Figure 5. The relationship between the bead displacement and the back-focal-plane image.

A quadrant photodiode is a sensor that can be used to measure these shifts in the intensity centroid. This sensor is composed of four independent photodiodes that each produces an electric current in proportion with the intensity of the light impinging on their respective active areas. A schematic diagram of a quadrant photodiode is shown in Figure 6.

13
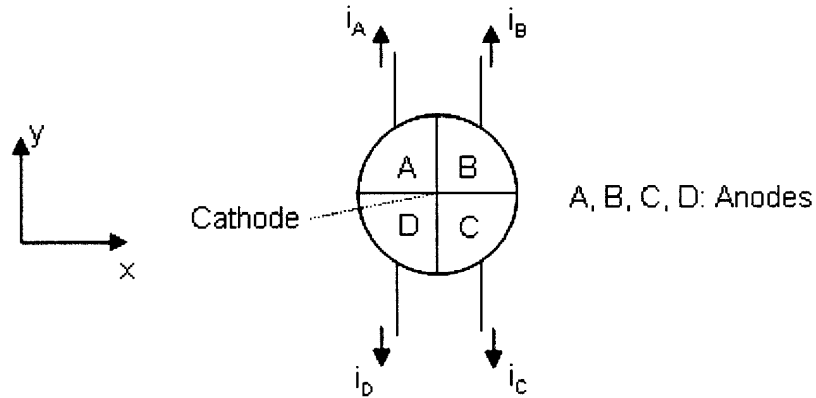
Figure 6. Schematic diagram of a quadrant photodiode.

A measurement of the displacement of the 'blob', as shown in Figure 5 above, along the x and y-axes is given by the following set of relationships:

$$x \propto (i_B + i_C) - (i_A + i_D)$$
$$y \propto (i_A + i_B) - (i_C + i_D)$$

Commercial quadrant photodiode modules (Figure 7) are designed with signal processing circuits that expect an intense laser beam spot in the active area. Because the back-focal-plane image is a 'blob' and the light intensity is relatively low ($\sim$0.5mW/cm^2), the signals obtained by using these commercial modules will be much too small to provide high resolution displacement information. Therefore, it is necessary to design a customized position sensing module for optical tweezers instruments.
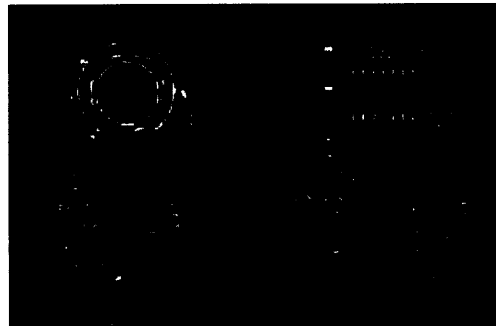
Figure 7. Position sensing module using a quadrant photodiode (PSS-QP50-6SD, Pacific Silicon Sensor Inc.).

A simple and inexpensive position sensing module will now be described. First of all, it is desirable to have a quadrant photodiode with as large an active area as possible. In this way, the back-focal-plane image projected onto the active area is as large as possible, which leads to a more pronounced movement of the 'blob' as the bead is displaced. Based on the operating principle of quadrant photodiodes, this larger movement of the 'blob' will lead to larger signal changes. In addition, because of the large size of the 'blob', the differences in intensity along the x and y-axes will be relatively small. Hence, the signal processing circuits will provide particularly high signal amplification. Figures 8 and 9 show schematic diagrams of a signal processing circuit designed for the SPOT-9DMI quadrant photodiode from UDT Sensors, Inc. Each component can be purchased from

14

most electronic component suppliers such as Digi-Key Corporation. The circuit design principles used were standard and can be found in many electronics textbooks (reference 5).
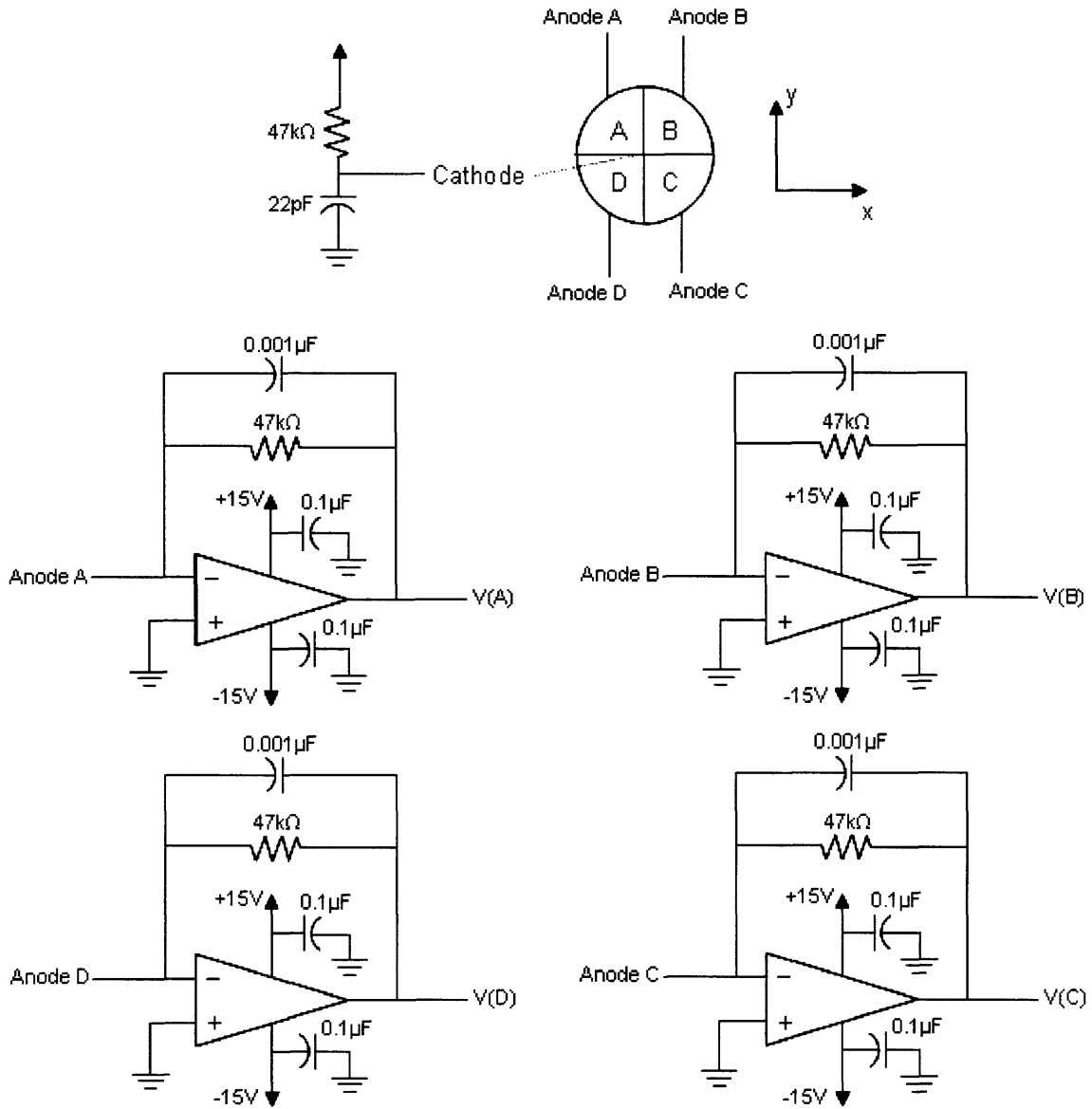
Figure 8. Schematic diagram of the current-to-voltage converter branch. As shown, each photodiode is reverse biased. The operational amplifiers are the OPA37 from Texas Instruments, Inc.
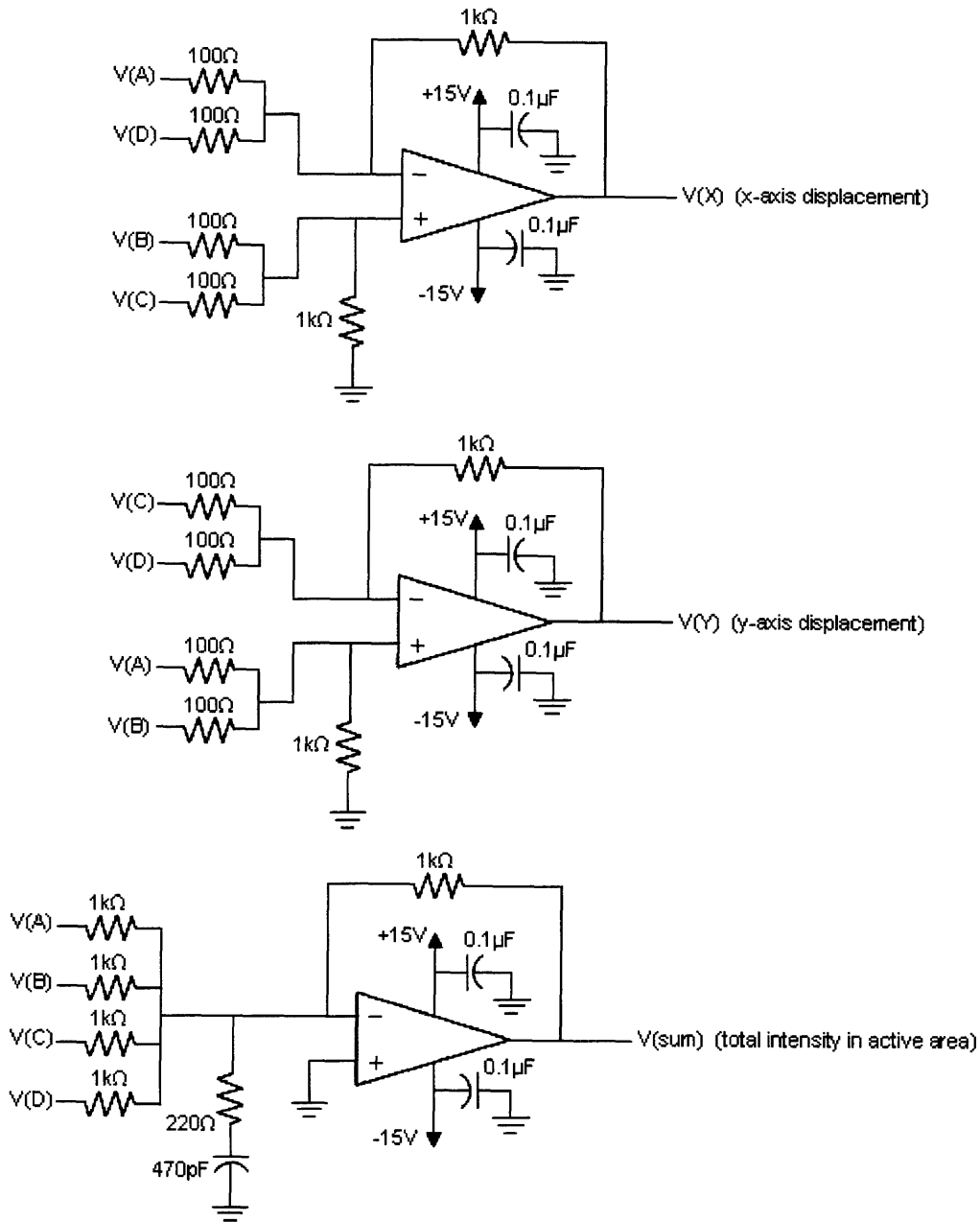
Figure 9. Schematic diagram of the arithmetic branch. Again, all operational amplifiers are the OPA37 from Texas Instruments, Inc. The signal V(sum) is used for normalization and to measure the bead's displacement along the beam axis.

This module provides nanometer displacement resolution and is currently being used in an undergraduate instrumentation course offered by the Biological Engineering Division at the Massachusetts Institute of Technology. It should be noted that because this module was customized for back-focal-plane displacement detection in optical tweezers, it will most likely not operate correctly for conventional applications such as laser beam spot tracking. A printed circuit board was designed using the free version of EAGLE, a popular layout program from CadSoft Computer, Inc. (Figure 10).
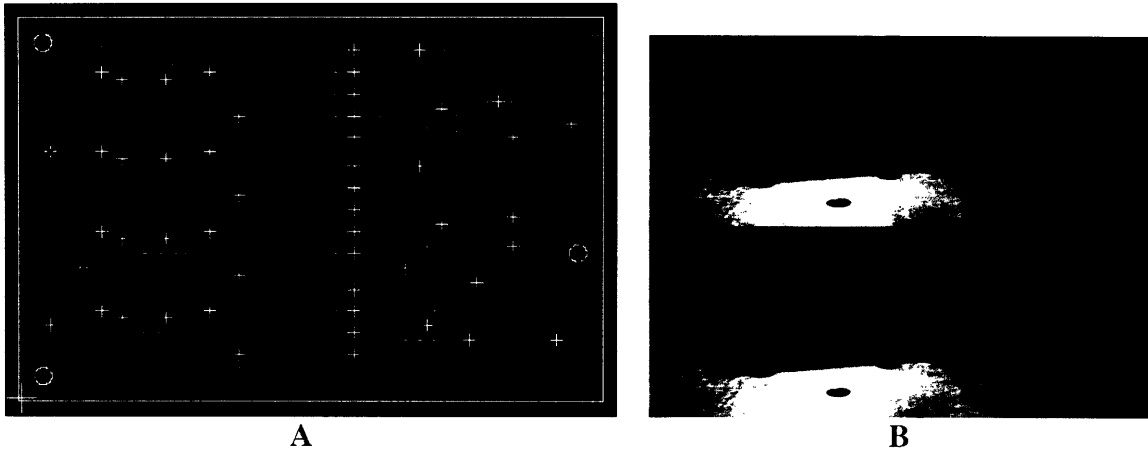
Figure 10. A Printed-circuit-board layout. B Quadrant photodiode and the assembled signal processing circuit.

The total cost of this module, including the quadrant photodiode, works out to be about $150. Commercial modules sell for more than $250, but end up not working anyway for optical tweezers applications without additional modifications. In addition, some photodiodes are not as sensitive to light in the near IR range and therefore have too small a bandwidth. The bandwidth becomes critical, for instance, when using the power spectral density method in measuring the trap spring constant. Reference 6 investigates this issue by looking at several sensor materials and designs. Incidentally, the position sensing module just described suffered from bandwidth issues. Future work will use a sensor optimized for near IR light like the Nd:YAG optimized quadrant photodiode from UDT Sensors, Inc.

A brief overview of the position calibration procedure will now follow. Since the position sensing module outputs two voltage signals, V(x) and V(y), corresponding to the two-dimensional displacement of the bead, a relationship between these measured signals and the displacement needs to be established. To do so, the bead is moved in a two-dimensional grid of known displacements while recording signals V(x) and V(y) at each grid point. A sample result of such a scan is shown in Figure 11. The central region of the grid clearly provides a one-to-one relationship between the measured signals and the displacement. Hence, one is now able to measure the displacement of the bead using the position sensing module.
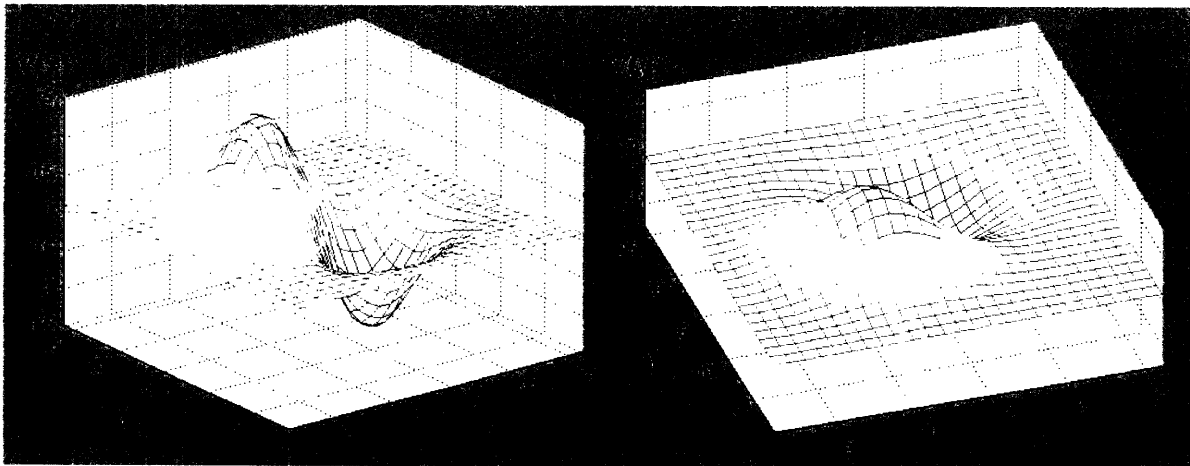
Figure 11. Signals V(x) and V(y) versus bead displacement (arbitrary units). Only the central region provides an unambiguous relationship between the measured signals and the displacement.

Chapter 2: Enhanced photobleaching of fluorophores in combined optical trapping and single molecule fluorescence spectroscopy

Combining the techniques of optical trapping and single molecule fluorescence enables the simultaneous application of force and observation of induced structural changes. There is a vast array of interesting experiments that can be performed with such a combination. For instance, Figure 12 shows a potential experiment combining optical tweezers and single molecule fluorescence resonance energy transfer (FRET). This experiment utilizes FRET to report local, intramolecular structural changes induced by an external force. Therefore, if fluorophores can be attached specifically to sites on a macromolecule, high resolution structural measurements can be made.
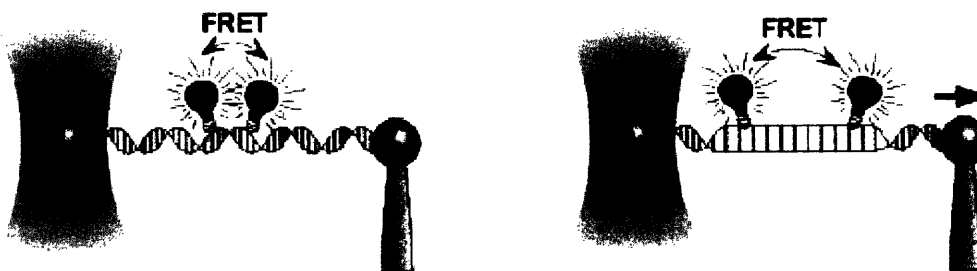
Figure 12. DNA mechanical stretching together with FRET (adapted from reference 7).

Ishijima et al. first demonstrated this combination of techniques at the single molecule level in 1998 (reference 8). By this time, both single molecule techniques were relatively well established such that a judicious choice of a few additional filters and dichroic mirrors was all that was needed to incorporate both techniques into a single instrument. Sample designs can be found in references 8 and 9. In their experiment, Ishijima et al. were able to simultaneously observe mechanical and ligand-binding/unbinding events in a single one-headed myosin molecule. A simplified schematic diagram of the experiment is outlined in Figure 13. The myosin molecule was immobilized onto a surface and the association/dissociation of a single Cy3-ATP ligand (Cy3 fluorophore conjugated to an ATP molecule) was observed using total internal reflection fluorescence (TIRF). An actin filament, held by a double trap, was brought close to the myosin molecule, enabling the actomyosin interaction. As shown schematically in Figure 13, the binding of Cy3-ATP causes myosin molecules to change conformation and unbind from actin. This mechanical actomyosin interaction was observed by measuring the displacement of one of the optical traps. A time trace of the simultaneous measurement of mechanical actomyosin interaction and Cy3-ATP ligand binding/unbinding is shown in Figure 14. The correlation is remarkably clear.
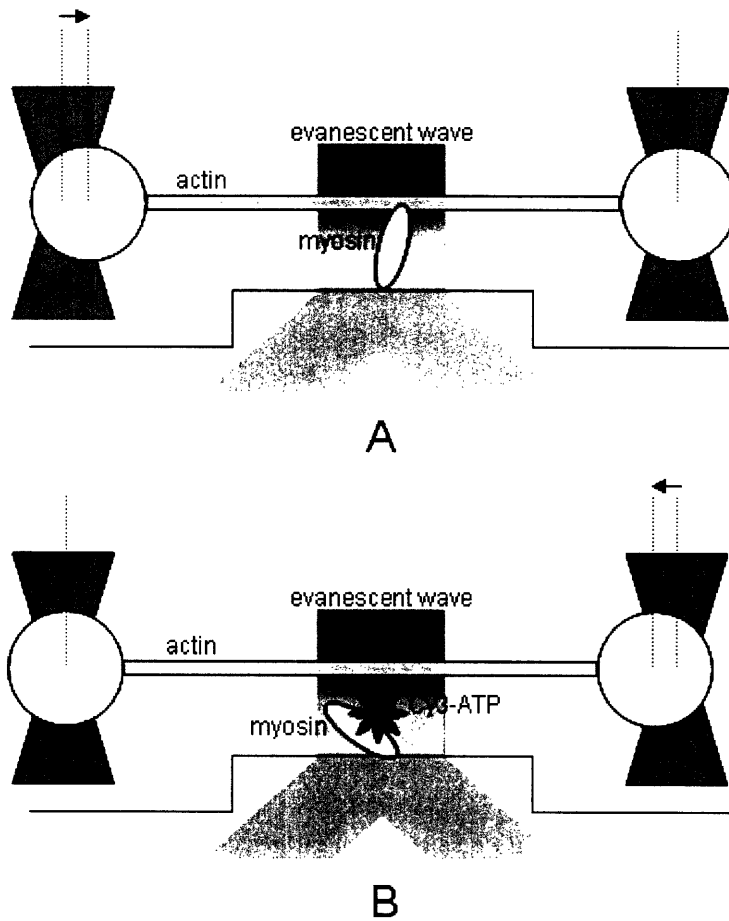
Figure 13. Schematic diagram of the experiment described in reference 8.
A Cy3-ATP ligand not bound to myosin. B Cy3-ATP ligand bound to myosin.
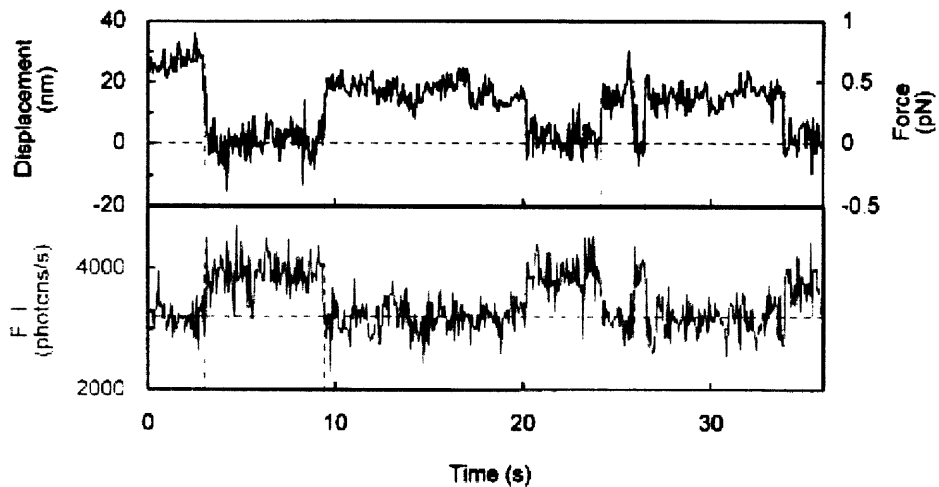
Figure 14. Simultaneous observation of mechanical and ligand binding/unbinding events. The bottom time trace is a measure of the photons emitted by a Cy3-ATP ligand bound to the myosin molecule.

Several years later, Lang et al. performed another experiment combining optical trapping and single molecule fluorescence (reference 9). A schematic diagram of their experiment is shown in Figure 15A. Optical tweezers was used to unzip two strands of DNA while TIRF was used to simultaneously detect the unquenching of two TMR fluorophores conjugated to the strand ends. A sample time trace of the mechanical and

19

fluorescent measurements is shown in Figure 15B. The sudden drop in the force time trace was due to the unzipping of the strands, causing the bead to jerk back into the middle of the trap. The simultaneous sudden rise in fluorescence was due to the unquenching of the two TMR fluorophores, also resulting from the unzipping event. The source of photons was the immobilized short strand, the one with the red dot (TMR fluorophore) attached to its 3' end in Figure 15A.

A	B
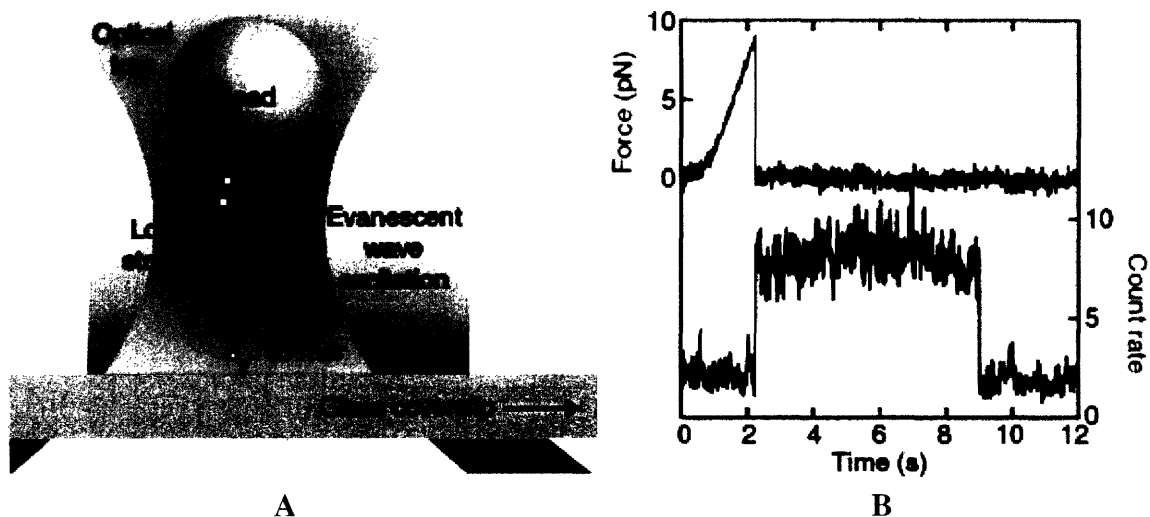
Figure 15. A Schematic diagram of the experiment described in reference 9. The red dots on the indicated 5' and 3' ends represent TMR fluorophores. **B** Simultaneous measurements of an unzipping event using optical tweezers and single molecule fluorescence (adapted from reference 9).

Because of the shortness of the DNA strands, the trapping beam overlapped with the fluorescence excitation region. Hence, the fluorophores were exposed to light from both the fluorescence and trapping laser. Lang et al. reported that the addition of the much more intense trapping laser enhanced the photobleaching of fluorophores, forcing them to use the TMR fluorophore which they found not to be adversely affected. In addition, it is not clear how many or how frequently they obtained such simultaneous unzipping detection measurements.

In a recent study performed by van Dijk et al., this enhanced photobleaching phenomenon was studied quantitatively with three key fluorophores used heavily in single molecule fluorescence research: Cy3, Alexa555 and TMR (reference 10). All three fluorophores were similar in the sense that they all excited very well at a wavelength of 532nm. A simplified schematic diagram of their experiment is shown in Figure 16A. A bead was coated with the fluorophore of interest and trapped using optical tweezers. To excite the fluorophores, the bead was also exposed to a fluorescence laser, which was collinear with the trapping laser. Because of the rotational diffusion of the trapped bead, all fluorophores were evenly bombarded with photons from both the trapping and fluorescence lasers. By keeping the power of the fluorescence laser constant, they investigated the relationship between the photobleaching rate and the trapping laser power.
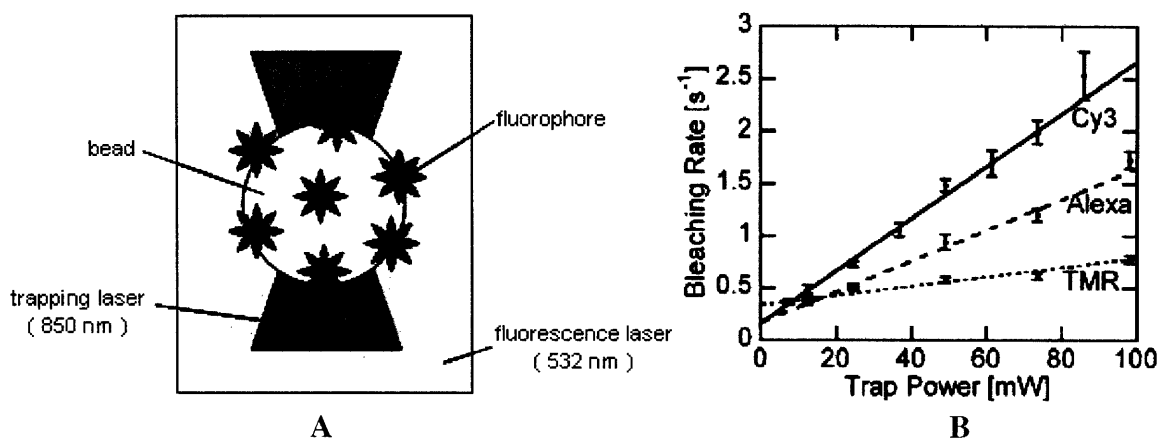
Figure 16. A Schematic diagram of the experiment described in reference 10. B Dependence of the photobleaching rate on trapping laser power (adapted from reference 10).

van Dijk et al. saw that the photobleaching rate increased with increasing trapping laser power. Their results, shown in Figure 16B, showed that Cy3 fluorophores were the most affected while TMR fluorophores were the least affected. The results of this study explicitly demonstrated the limitation of simply combining optical trapping and single molecule fluorescence, as was done by the work discussed in references 8 and 9.

In the same work, van Dijk et al. showed that the new photobleaching pathway introduced by the trapping laser was due to the simultaneous bombardment of fluorophores by photons from the fluorescence and trapping laser. To show this, the researchers chopped the fluorescence laser while keeping the trapping laser on at all times (Figure 17A). Their results, shown in Figure 17B, demonstrated that the trapping laser alone was not the cause of the enhanced photobleaching. The inset in Figure 17B shows a relatively smooth decay curve with the periods without fluorescence excitation cut out. Based on these results, a model was proposed, as shown schematically in Figure 18A. The near infrared (NIR) photons from the trapping laser appeared to be taking excited fluorophores up to another excited state, where the fluorophores were prone to photobleach along a new and significant destruction pathway.
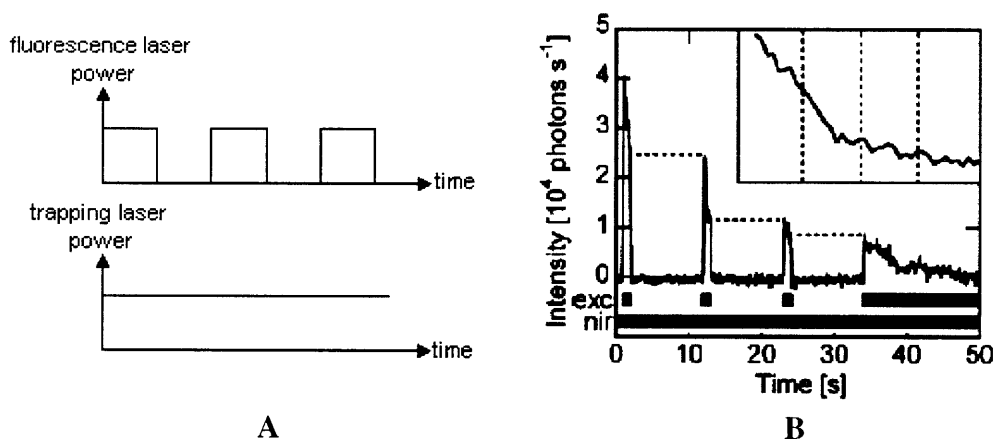
Figure 17. A Time traces of fluorescence (chopped) and trapping laser power. B Photon counts from a coated bead. In the inset, the times without fluorescence excitation were cut out (adapted from reference 10).

21
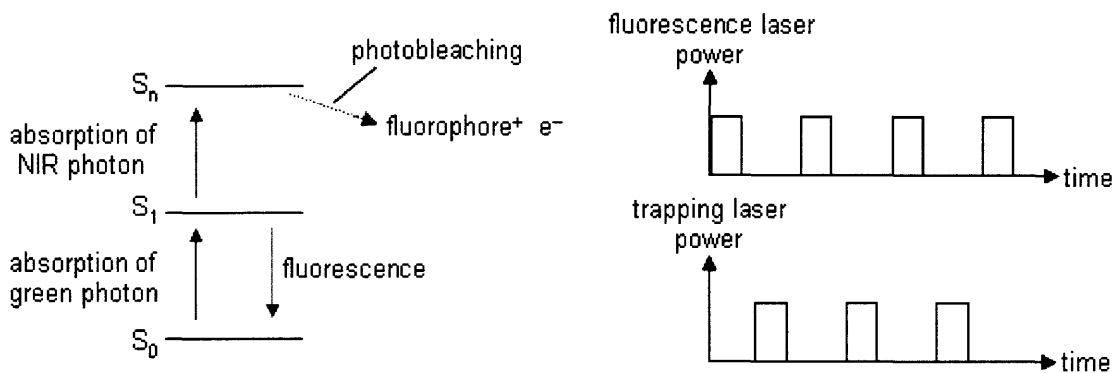
Figure 18. **A** Proposed model for the new photobleaching pathway. **B** Time traces of the fluorescence and trapping lasers synchronously chopped.

These results immediately suggest a simple method of eliminating this new photobleaching pathway. The basic idea is illustrated in Figure 18B. If the fluorescence and trapping lasers are synchronously chopped as shown, the new photobleaching pathway is avoided. The remainder of this chapter will discuss the design of a straightforward and noninvasive module to achieve this. This synchronized chopping module can be easily incorporated into a modern instrument combining optical trapping and single molecule fluorescence.

First of all, the appropriate beam chopping device must be decided on. The chopping frequency is of utmost importance for the trapping laser because of the thermal motion of the bead in the absence of the trap. If the frequency is too low, the bead may diffuse away during the trap off-times. Even if the frequency is high enough to keep the bead trapped, it may be slower than the higher frequency dynamics of the bead. In effect, the bead may experience a noticeable jolt of force at the chopping frequency. Figure 19 shows a time trace of a trapped bead's position in one axis with the trapping laser chopped at a seemingly high 250Hz. The average power of the trapping laser was set at a typical value of 100mW. It was noticed that during the times the trapping laser was off, the bead diffused away a little bit and then was jolted back to its equilibrium position when the trapping laser turned back on again. In an experiment, such sudden jolts in position are undesirable.
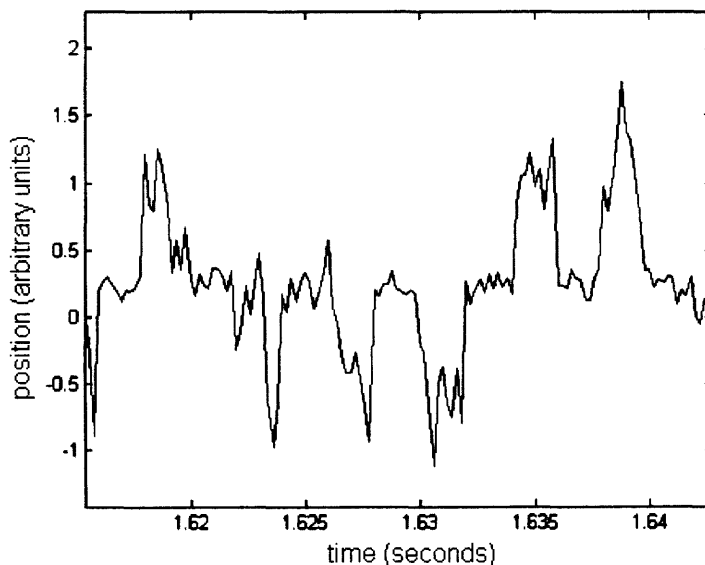
Figure 19. Time trace of the bead's position along one axis. The trapping beam was chopped at 250Hz. The period of the jolts in the bead's position is clearly 0.004 seconds.

22

Based on these results, it is clear that the chopping frequency must be set high enough such that the beam appears continuous relative to the bead's dynamics. Furthermore, if the bead is being pulled out of the trap like in the DNA unzipping experiment shown in Figure 15A, the situation is worsened and must be reconsidered. Figure 20 shows a time trace of a trapped bead's position in one axis with the trapping laser chopped again at 250Hz and set at a power of 100mW. Starting at approximately 1.85 seconds, fluid was flown past the bead to invoke a viscous drag force. With the addition of this external force, the position jolts were more pronounced. During the trap off-times, the bead was being driven out of its equilibrium position with the unbalanced viscous drag force.
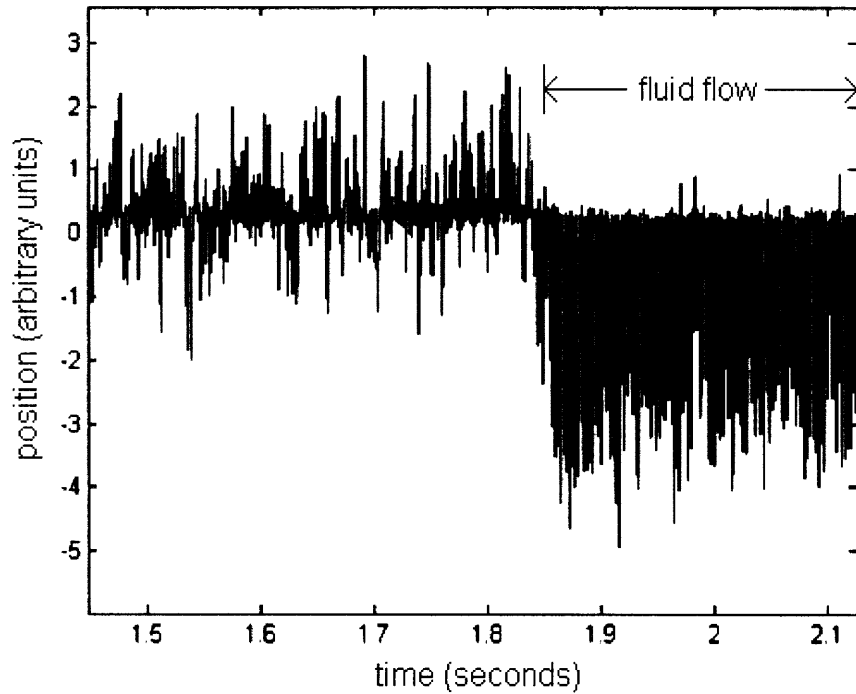
Figure 20. Time trace of the bead's position along one axis. The trapping beam was chopped at 250Hz. Commencing at about 1.85 seconds, the bead experienced a viscous drag force.

It is found that a minimum chopping frequency of 10kHz is necessary to maintain the integrity of the trap under conditions where external forces are involved (reference 11). At such high frequencies, an acousto-optic-deflector (AOD) represents a sensible choice as a chopping device. AODs are solid-state devices that are composed of a crystal of transparent acousto-optic material (ex. tellurium dioxide) with a piezoelectric transducer bonded to one end and an acoustic absorber bonded to the opposite end to suppress reflected acoustic waves (Figure 21).
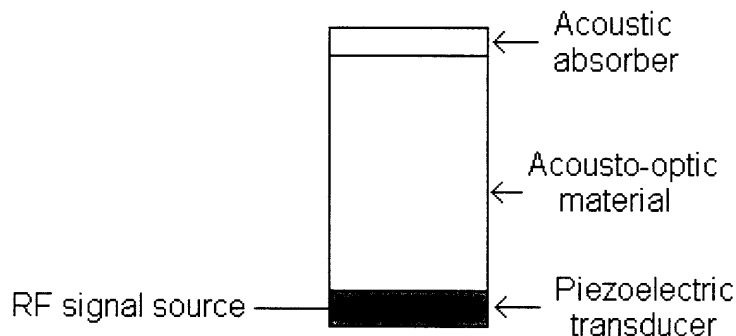
Figure 21. Schematic diagram of an AOD.

23

During operation, an RF voltage signal is applied to the piezoelectric transducer which causes the piezoelectric material to expand and contract at the signal frequency. Because this transducer is coupled to the acousto-optic material, acoustic/sound waves are generated in the material. Hence, there are periodic variations in the refractive index that ultimately behaves as a diffraction grating. If a laser beam passes through the material, as shown schematically in Figure 22, a portion of the incident beam is diffracted/deflected at various discrete angles. The first order diffraction maximum is the most intense and is therefore used as the core beam for an instrument utilizing AODs. Since the acoustic velocity is constant in the material, a change in the RF signal frequency translates to a change in the grating spacing and hence a change in the deflection angle θ of the first order diffraction maximum.
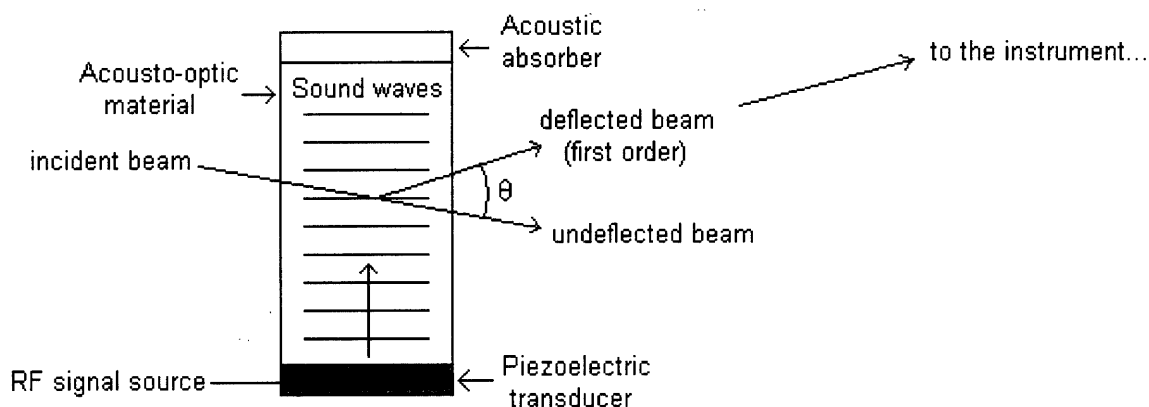
Figure 22. Schematic diagram of an AOD in operation.

Because of the ideal properties of low drift and noise, no creep, high speed and great resolution, AODs are typically incorporated into modern optical tweezers instruments to steer the trapping beam. A schematic diagram of a modern optical tweezers instrument combined with single molecule fluorescence is shown in Figure 23 (reference 9). To achieve two-dimensional steering of the optical trap in the specimen focal plane, two perpendicularly-aligned AODs are used. Commercial two-dimensional AOD modules designed for optical tweezers applications are available with easily controllable RF signal sources. The module used in this work was the DTD-274HA6 2-Axis Deflector from IntraAction Corp.

AODs have a very quick response time and are therefore readily used as laser beam chopping devices. The basic idea behind the chopping operation is shown schematically in Figure 24. Since an RF signal is required to create the first-order deflected beam (core beam used in the instrument), turning this signal source on and off amounts to chopping the deflected beam. To synchronously chop the fluorescence and trapping lasers as shown in Figure 18B, AOD modules are required for both these beams. Because a two-dimensional AOD module for the trapping beam is normally already incorporated into the instrument (Figure 23), an additional AOD for the fluorescence beam is all that is needed. Since the cost of such an AOD is roughly $500, other uses besides chopping should be considered. The intensity of the fluorescence, for instance, can be easily controlled in real time by altering the amplitude of the RF signal source. In addition, the fluorescence excitation region can be moved around by steering the fluorescence beam with the AOD.

Figure 23 diagram labels:

S3

Lamp

P

QPD

F

Z

Piezo stage

X

Optical tweezers
and position

Single-molecule fluorescence

D

Intensified camera

Video camera

S1   F1

SAPD

z
y
z
x
x
y

L2

B   D

Pinhole

F2 S4

L1

S2

AODs

SAPD   D1   FM2   FM1   L3

Excitation laser   Trapping laser   Detection laser

Figure 23. Schematic diagram of an instrument combining optical trapping and single molecule fluorescence. The large red arrow is pointing to the two perpendicular AODs (adapted from reference 9).

RF Signal

ON   OFF   ON   OFF   ON

Sound waves

incident beam

deflected beam (first order)

θ

undeflected beam

incident beam

undeflected beam

RF signal ON

RF signal OFF
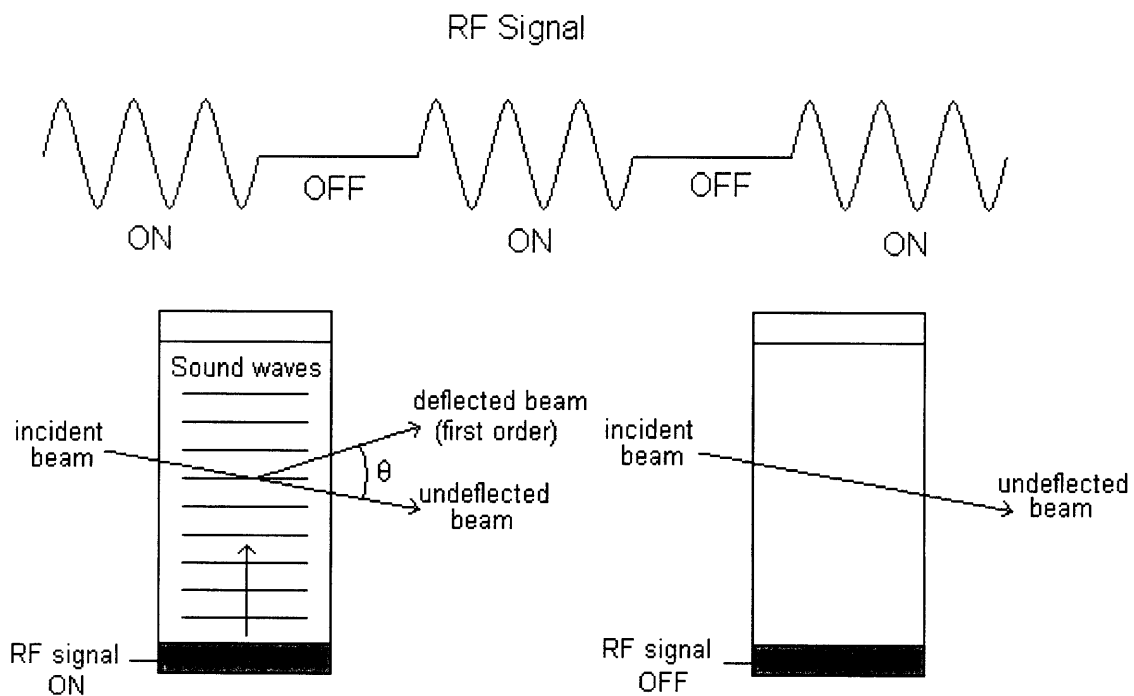
Figure 24. The basic principle behind chopping a laser beam with an AOD.

25

A description of the synchronized chopping module now follows. Figure 25 shows a schematic diagram of the part of the instrument relevant to the chopping module. The additional AOD for the fluorescence laser has been included.
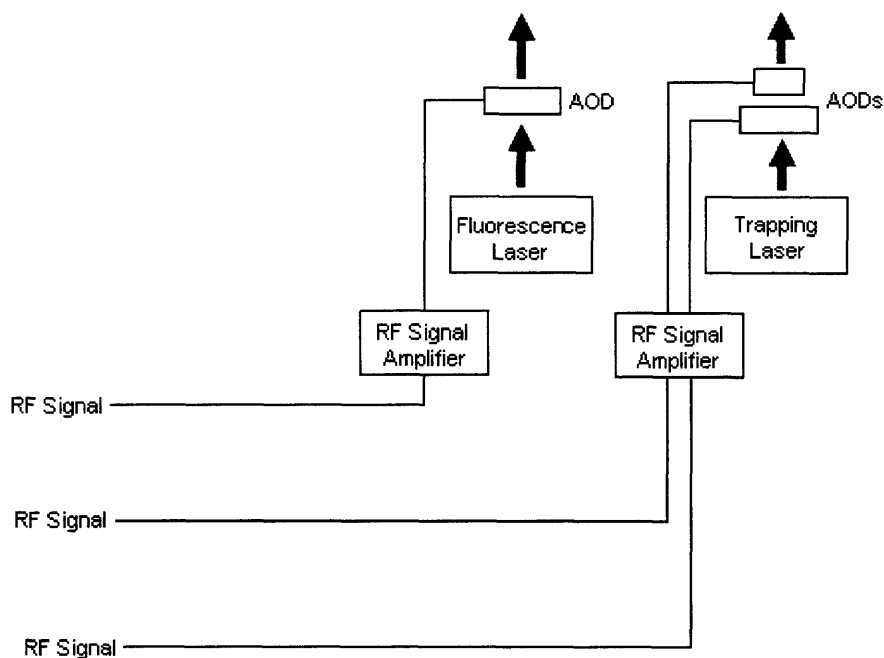
Figure 25. Schematic diagram of instrument part relevant to chopping.

Figure 26 shows a schematic diagram of this instrument part modified to enable synchronized chopping of the fluorescence and trapping beam.
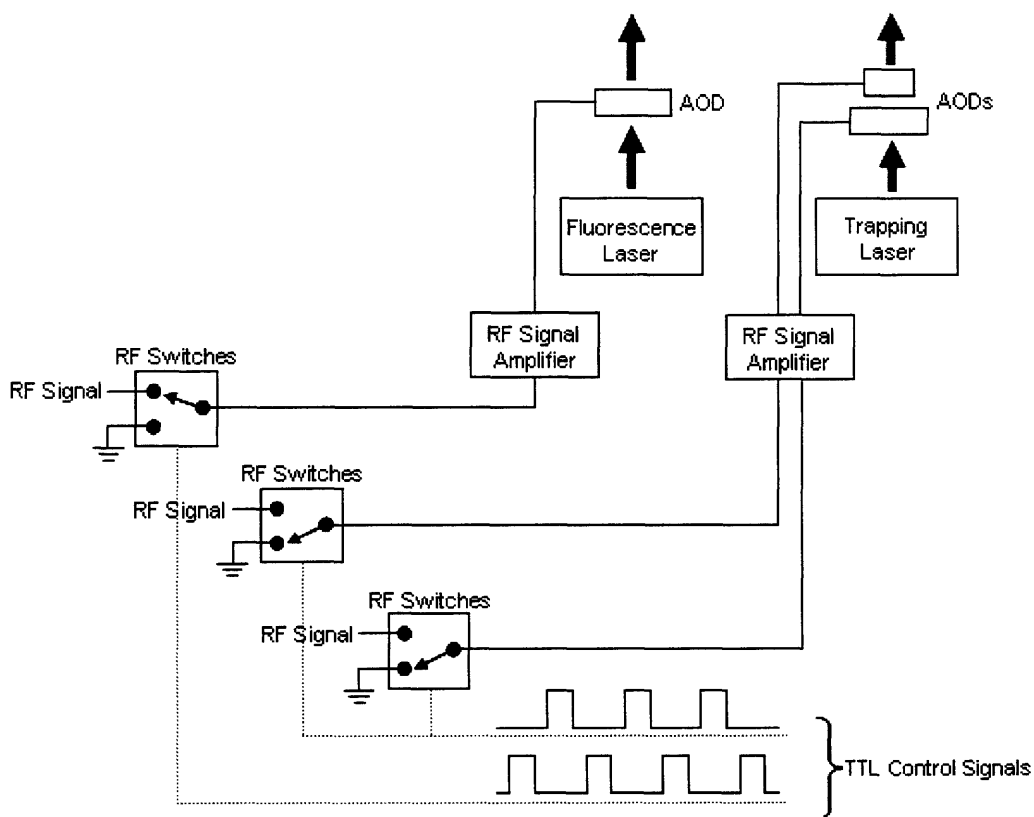
Figure 26. Schematic diagram of instrument portion modified for chopping.

The RF switches used were the MAX4567 integrated circuits (ICs) from Maxim Integrated Products, Inc. The MAX4567 IC contains two single-pole/double-throw (SPDT) CMOS switches that are designed for switching RF and video signals from DC to 350MHz. These standard ICs cost only a few dollars and have a switching time of less than 100ns. A TTL control signal is used to control which input signal is connected to the output line of the switch. Hence, sending a TTL pulse train switches the output between the RF signal and ground as shown in Figure 24.

To provide a synchronized pair of TTL control signals, a two channel function generator can be used. This, of course, is an overly elaborate and expensive solution to a simple problem. A far more flexible and inexpensive solution is the use of a programmable logic IC. Before the advent of programmable logic, custom logic circuits were built with standard off-the-shelf components. If there was a flaw in the design, the circuit and PCB needed to be redesigned and remade. But with programmable logic ICs, such as the field programmable gate array (FPGA), any customized logic circuit can be easily programmed into a single IC. A programmable logic IC is composed of a regular structure of logic cells or modules and interconnects that are appropriately hardwired during programming to implement the designer's custom logic circuit. Circuits such as traffic-light controllers and photon counters can be implemented with ease. And if the design is flawed, the designer simply needs to reprogram the IC with the corrected design. Hence, the real value of programmable logic is in its increased flexibility without compromising speed.

To create the TTL control signals for the chopping device, the Xilinx Spartan-3 FPGA was used. To shorten development time, a powerful and self-contained development board was purchased from Digilent, Inc. at a cost of only $100. This Spartan-3 starter board permitted straightforward experimentation with the Xilinx Spartan-3 FPGA. A picture of the board is shown in Figure 27.
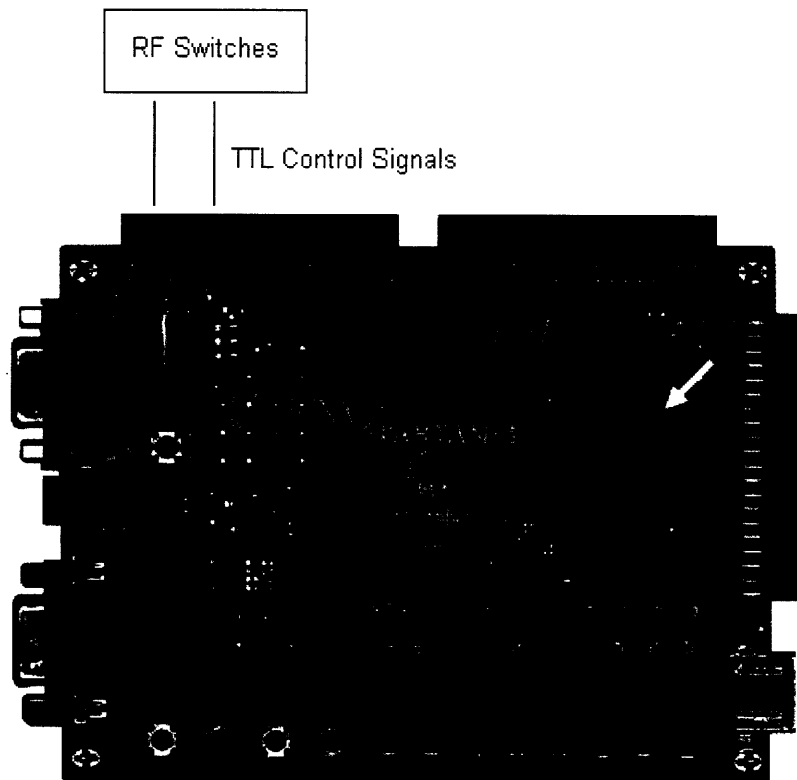
Figure 27. Spartan-3 FPGA starter board from Digilent, Inc. The FPGA IC is marked by the white arrow.

The board provides access to several I/O ports for interfacing to other devices. For the synchronized chopping module, the FPGA IC was interfaced to the RF switches, as shown schematically in Figure 27. To design and test the logic circuit and then download the design onto the board, the latest free ISE WebPACK design tool software from Xilinx was used. A schematic diagram of the circuit implemented is shown in Figure 30. The functional blocks used are standard and their detailed design can be found in any modern digital electronics textbook (reference 12). As indicated in the circuit diagram, there are four 16-bit parameters, P1, P2, P3 and P4, that the user can specify in order to generate the desired TTL control signals. Figure 28 shows the meaning behind these four parameters.

T1 = P1 · 20ns   T2 = P2 · 20ns   T3 = P3 · 20ns   T4 = P4 · 20ns
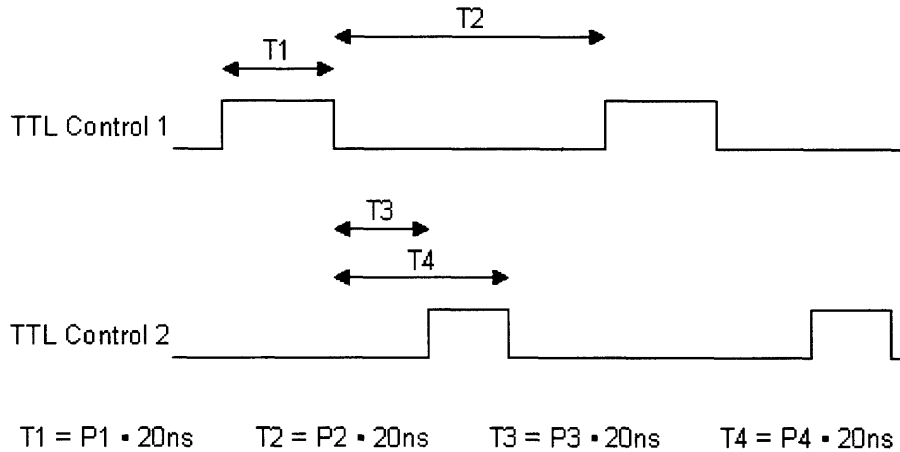
Figure 28. Parameters for two synchronized TTL control signals.

Since the onboard clock is 50MHz, the time resolution (period of a clock cycle) is 20ns. And with 16 bits allocated to each parameter, a time constant as high as 1.31ms can be specified. This range of times is sufficient for pulse train frequencies of 10kHz or higher. A sample simulation result is shown in Figure 29.

Figure 29. Simulation results from ModelSim XE II component of Xilinx ISE WebPACK design software.
P1 = 5 (binary: 0000000000000101)
P2 = 10 (binary: 0000000000001010)
P3 = 3 (binary: 0000000000000011)
P4 = 5 (binary: 0000000000001010)

28
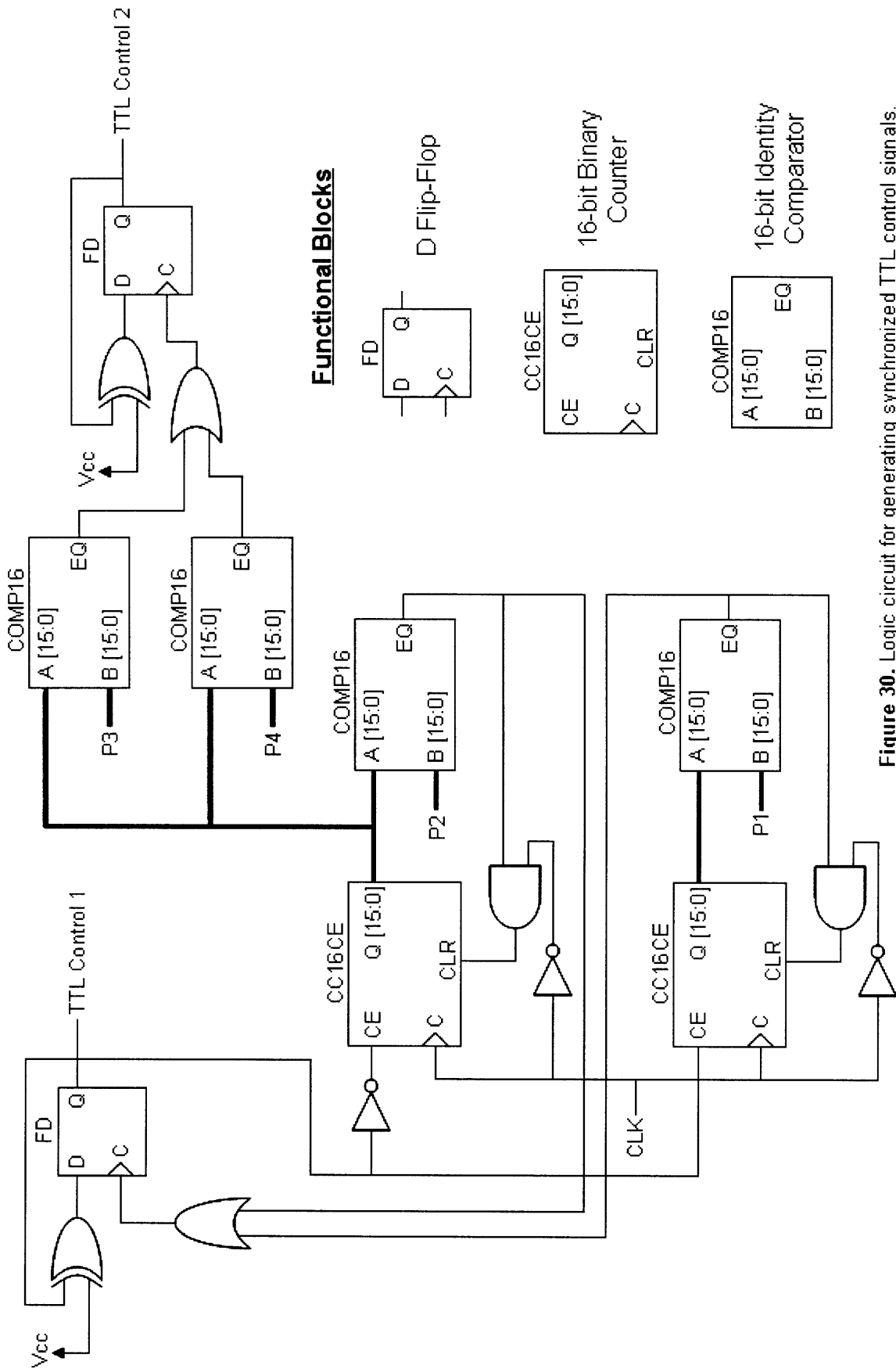
Figure 30. Logic circuit for generating synchronized TTL control signals.

Functional Blocks

D Flip-Flop

16-bit Binary Counter

16-bit Identity Comparator

29

This circuit design does not represent the only or even the best solution to the problem of generating two synchronized TTL control signals, but it works and is easy to implement. One may also make the argument that using an FPGA IC is an overly elaborate solution to a simple problem. The counter argument is, of course, that many other logic circuits can be implemented on the same FPGA IC. For instance, one can implement several photon counters and provide high-speed control over a myriad of other TTL controllable devices on the instrument. Furthermore, all these circuits can be synchronized with each other because they are all running under the control of the same onboard clock.

To test the functionality of the synchronized chopping module, a photodiode was placed in the path of the fluorescence and trapping beam after the AODs. A sample oscilloscope trace of the two photodiode signals is shown in Figure 31. Here, the chopping frequency was set at 10kHz.

Figure 31. Oscilloscope trace of photodiode signals
(top trace: trapping beam, bottom trace: fluorescence beam).

The integrity of the optical trap was next tested. A comparison was made between having the trapping laser in continuous mode and chopping mode. The chopping frequency used was 10kHz and the average power for both modes was set the same. It was found that the integrity of the optical trap was not compromised in the chopping mode as shown qualitatively in Figure 32. Here, a trapped 560nm-diameter bead experienced viscous drag forces in the forwards and backwards directions along one axis. The bead displacements along this axis were found to be similar in both modes. More importantly, the optical trap in the chopping mode was able to apply high forces on the bead.
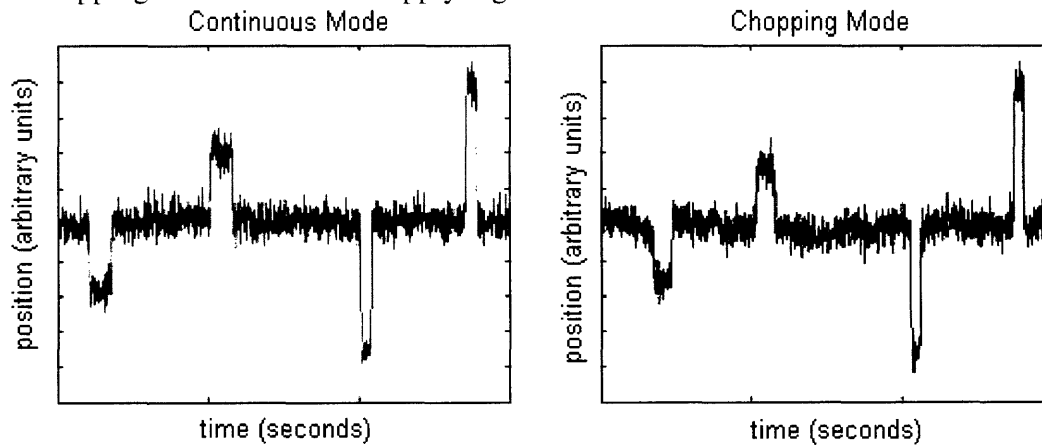
Figure 32. Bead displacement time traces along one axis. Periods of applied viscous drag force are represented by sudden periods of noticeable displacements from the equilibrium.

Sample results from further tests are shown in Figure 33. Figure 33A shows the measured intensity profile of the trapping beam cross-section in both the continuous and

chopping modes. Figure 33B shows the results of a calibration procedure performed to determine the spring constant of the optical trap. Here, the Stokes' flow method was used. Results obtained under both the continuous and chopping modes were very similar.
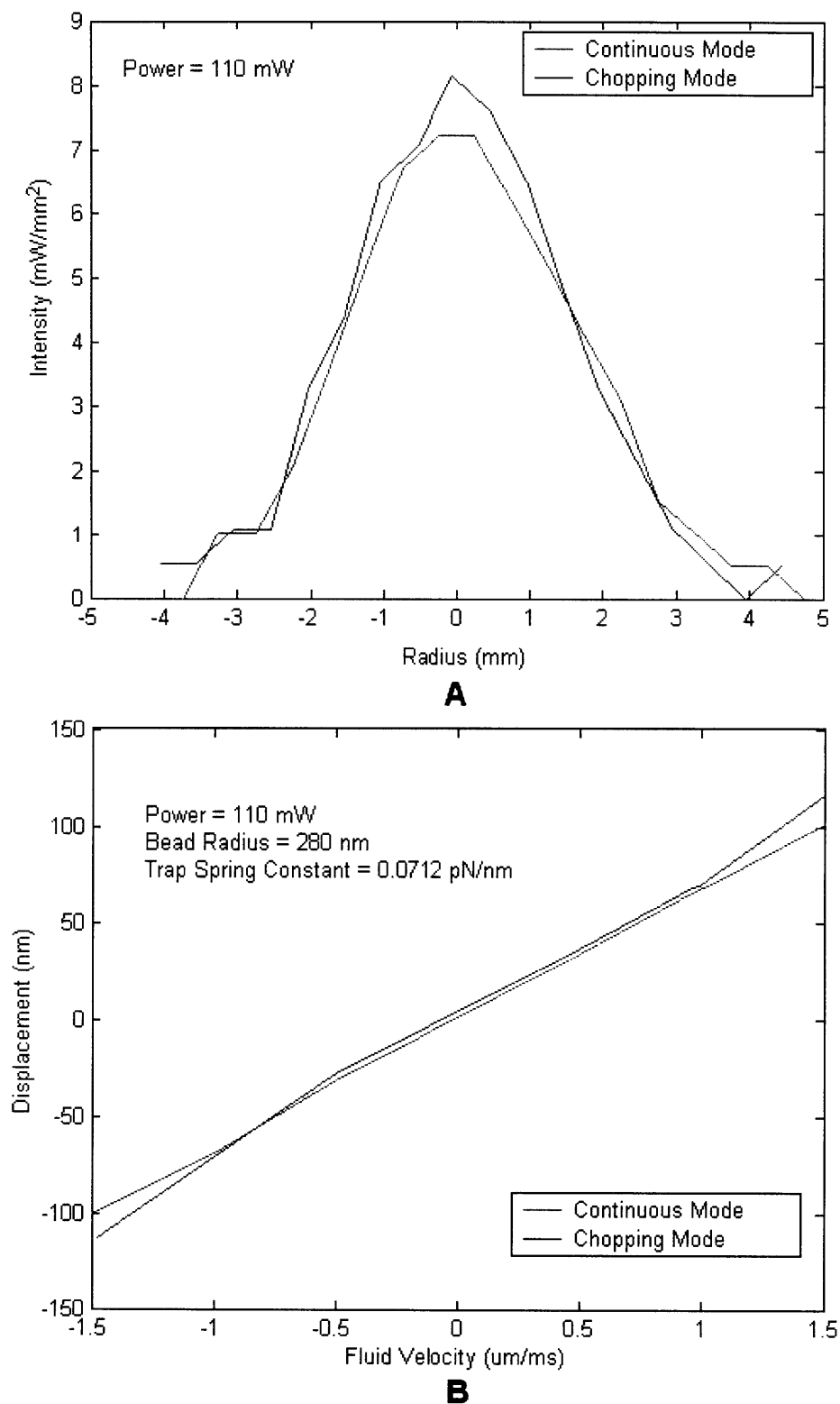
Figure 33. **A** Intensity profile of the trapping beam cross-section. **B** Spring constant calibration results using the Stokes' flow method.

31

The purpose of the synchronized chopping module is to extend the lifetime of fluorophores by avoiding the photodestructive pathway introduced by the trapping beam, as modeled in Figure 18A. A discussion of several tests performed to determine the improvements made with this module will now follow.

A clear illustration of the trapping beam's detrimental effect and of the improvements afforded with using the synchronized chopping module is shown in Figure 34. In this experiment, the surface of a coverslip was coated with Cy3 fluorophores and excited with TIRF using a 532nm fluorescence beam. Figure 34A shows the photobleaching of fluorophores under the influence of only the fluorescence beam. Figure 34B shows the dramatic effect of the trapping beam (1064 nm) when both the fluorescence and trapping beams are turned on simultaneously. The surface area exposed to the trapping beam photobleached almost instantaneously. In Figure 34C, the improvement made by synchronously chopping both beams is clearly seen. For all results shown, the fluorescence and trapping beam powers were set at 130μW and 90mW, respectively.
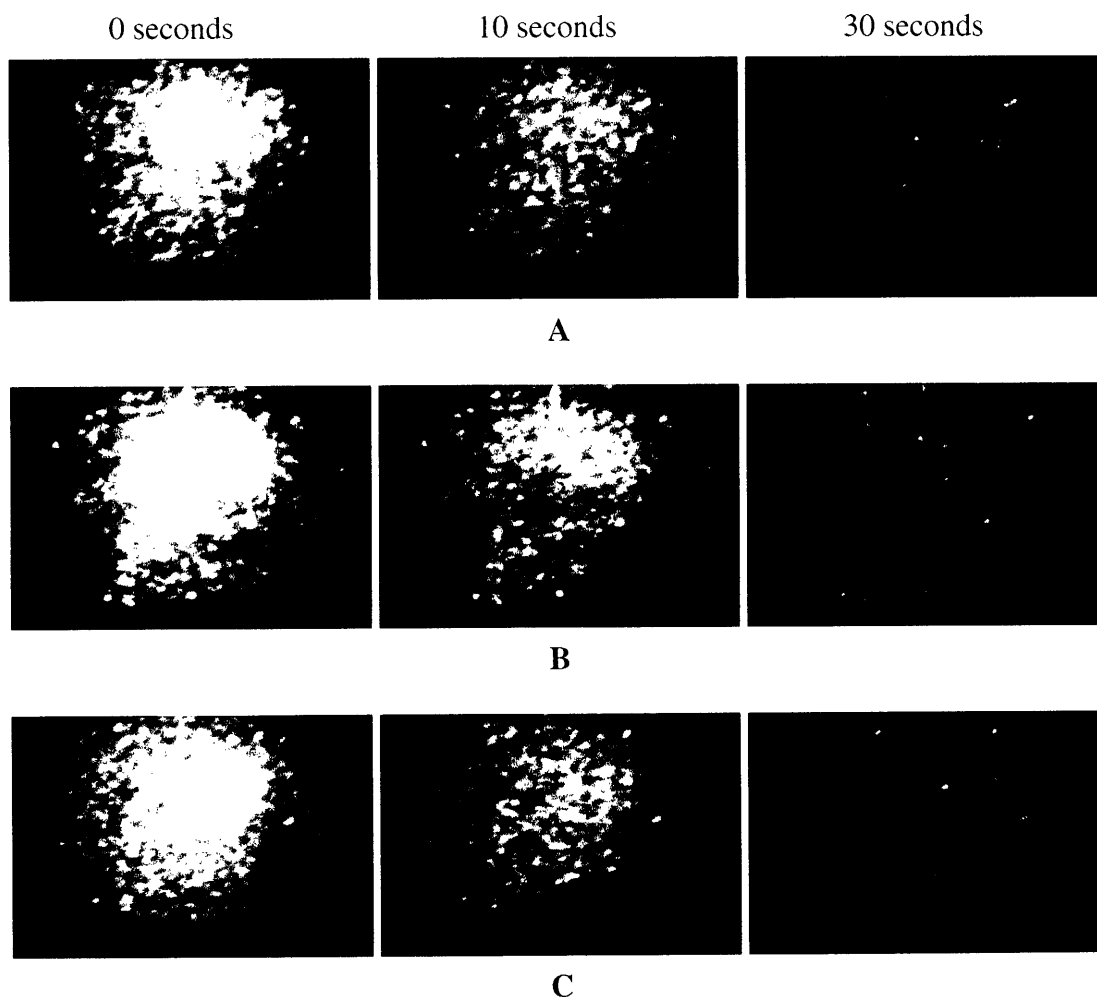
Figure 34. Figure captions from fluorescence movies. A Only the fluorescence beam is turned on. B The fluorescence and trapping beams are turned on simultaneously (location of trapping beam indicated by black arrow). C The fluorescence and trapping beams are synchronously chopped.

To quantify improvements made in extending the lifetime of fluorophores, a set of experiments similar to that of van Dijk et al. (reference 10) was performed. Beads were coated with the fluorophore of interest and trapped with a 1064nm trapping laser, as shown in Figure 16A. To excite the fluorophores, a 532nm fluorescence laser was used. The same set of fluorophores, Cy3, Alexa555 and TMR, was used in this study. The goal of these experiments, however, was to compare the lifetime of the fluorophores under the continuous and chopping modes. Sample results for all three dyes are shown in Figure 35, 36 and 37. Under both modes, the average trapping and fluorescence laser powers were set at 110mW and 200μW, respectively. The chopping frequency was 10kHz and photon counting was performed with 100ms binning. The buffer solution used was 0.5% beta-mercaptoethanol in ddH$_2$0.
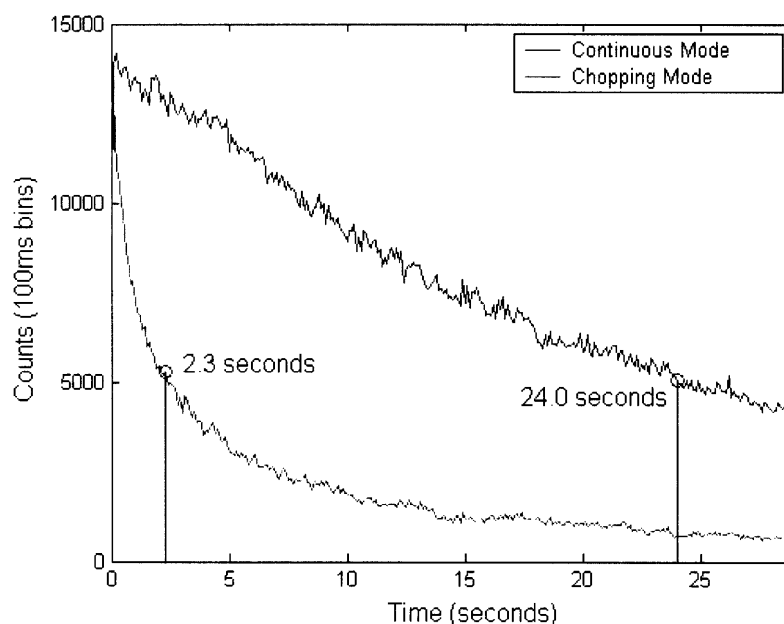
Figure 35. Cy3 fluorescence decay curves.
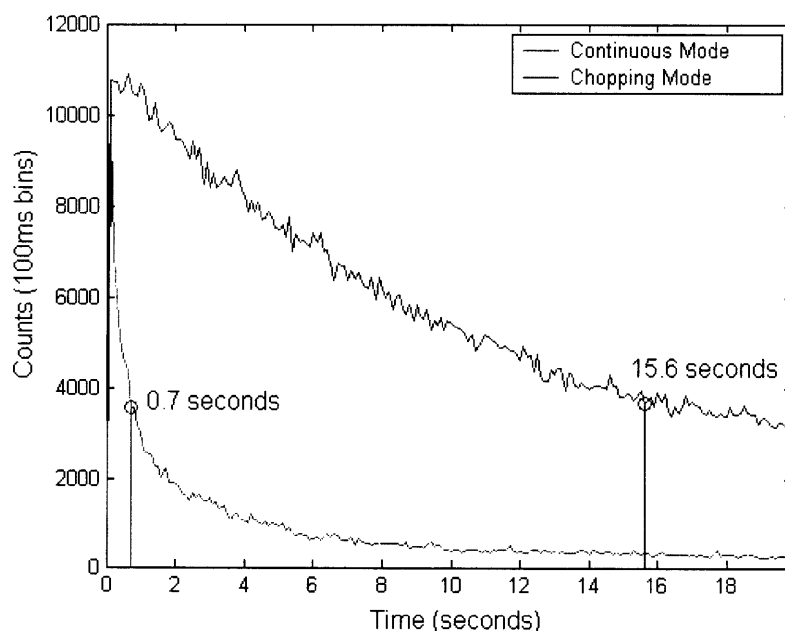
Figure 36. Alexa555 fluorescence decay curves.
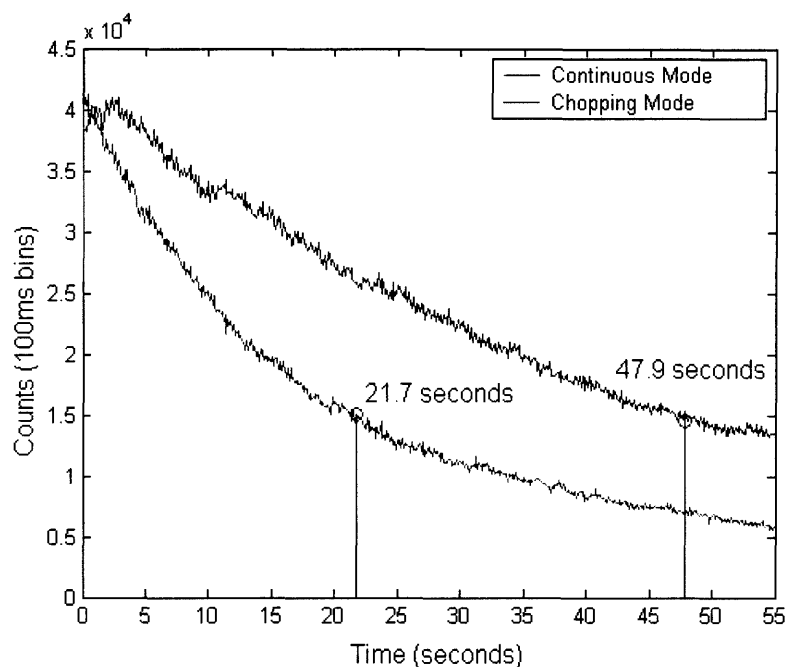
Figure 37. TMR fluorescence decay curves.

The results just shown clearly demonstrate the significant improvements made in extending the lifetime of fluorophores in the presence of both the fluorescence and trapping lasers. This simple synchronized chopping module proved to be a quick and inexpensive solution to this major bottleneck in experiments combining optical trapping and single molecule fluorescence. However, despite avoiding the destructive pathway shown in Figure 18A, this module cannot resolve the photodestruction caused by two-photon absorption. In order to produce a significant number of two-photon absorption events, the photon density must be approximately one million times that required to generate the same number of one-photon absorptions. Because the intensity of the trapping laser is many orders of magnitude greater than that of the fluorescence laser, two-photon absorption events will play a non-negligible role in the photobleaching of fluorophores. Alexa555 was found to suffer from this two-photon absorption process while the other two dyes were negligibly affected.

Chapter 3: Probing mechanotransduction phenomena with the ZIF268 protein-DNA system

Since the discovery of the structure of DNA by Watson and Crick in 1953, research has shown that DNA is much more than just an informational storage molecule. In particular, the mechanical properties of this remarkable molecule have proven to be crucial to proper cell function. For instance, Goodman et al. performed experiments to investigate whether the induced bending of DNA upon protein binding is important in itself or just a consequence of the way the protein binds to DNA (reference 13). The researchers probed the bacteriophage λ integration system and studied a DNA-binding protein IHF that is necessary for the recombination and was also known to bend DNA. They reasoned that if changing the shape of DNA was the protein's primary function, they could retain recombination by replacing the protein and its DNA binding site with an unrelated protein-DNA system known to bend DNA in a similar fashion. Not only did this replacement yield significant recombination, but to accentuate their point, they replaced the original DNA binding site with an intrinsically bent DNA segment and still found recombination to occur. For replacements that did not bend DNA, recombination was disabled.

In another study, Parvin et al. investigated the potential significance of DNA topology and conformation in transcriptional control (reference 14). The researchers studied the TATA-binding protein (TBP) which binds to the minor groove of the TATA element with the DNA bent significantly towards the major groove. By using a constrained minicircle strategy, where the site was pre-bent towards the major groove, they found a 100-fold increase in binding affinity compared to unbent (linear) DNA of identical sequence.

The study of protein-DNA interactions is essential to understanding basic cellular functions. In particular, the C_2H_2 zinc fingers are the most prevalent class of DNA-binding domains found in human transcription factors (reference 15). Each zinc finger is approximately 30 amino acids long and contains two conserved cysteines and two conserved histidines. These residues coordinate a zinc ion that enables the finger to fold compactly into a structure containing a β-turn and an α-helix (Figure 38A). As shown in Figure 38B, zinc finger proteins (ZFPs) are typically composed of two domains: the DNA-binding domain (array of zinc fingers) and the functional domain that performs actions such as gene regulation.

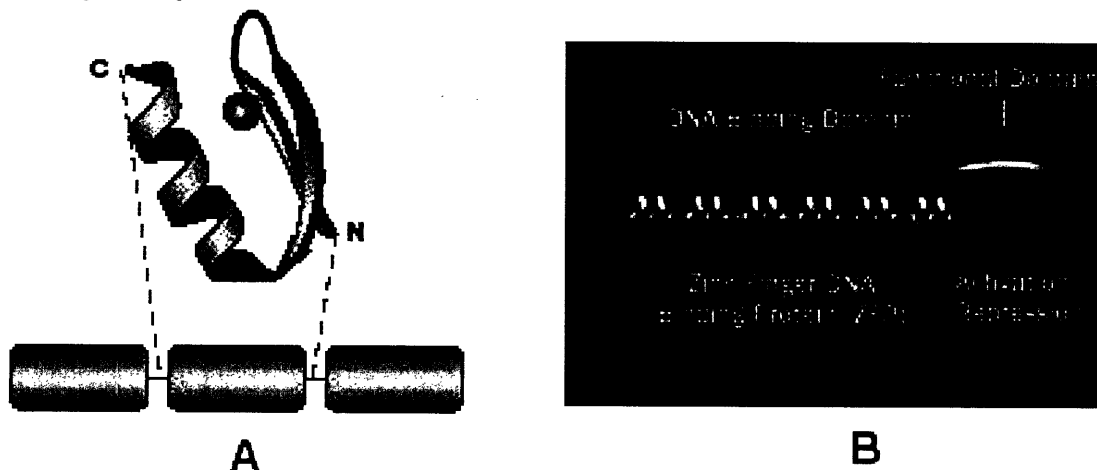
A   **B**

Figure 38. A Ribbon drawing of a single zinc finger, where the small orange sphere represents a zinc ion (adapted from reference 15). **B** Cartoon representation of a zinc finger transcription factor (adapted from www.sangamo.com, the website for Sangamo BioSciences, Inc.).

35

The first detailed structural information on how individual zinc fingers interact with their DNA binding site was obtained by x-ray crystallographic data on the ZIF268 protein-DNA complex (reference 16). The DNA-binding domain of the ZIF268 protein is composed of three sequential zinc fingers that recognize a specific DNA sequence of nine base-pairs, where each finger interacts with a three-base-pair subsite. In this study, Pavletich et al. showed that the three fingers are arranged in a semicircular structure that fits snugly into the major groove of B-form DNA as shown in Figure 39A. It was also shown that residues from the N-terminal portion of each α-helix make the primary contacts with the base pairs in the major groove (Figure 39B). A summary of the key protein-DNA interactions is shown in Figure 39C.
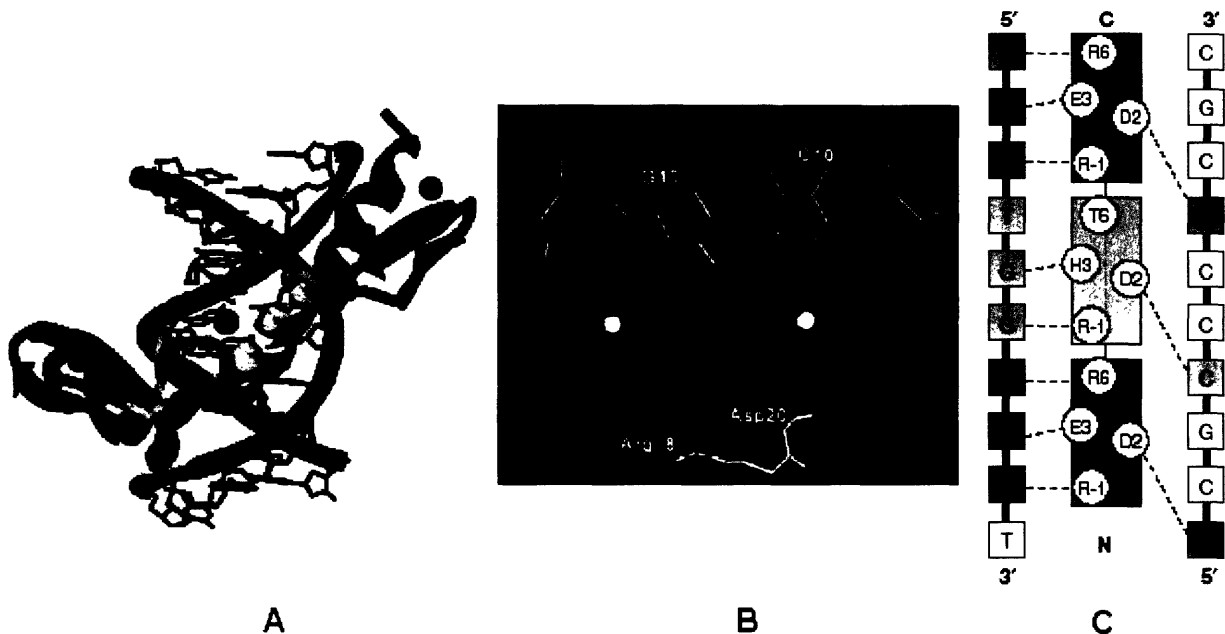
A   B   C

Figure 39. A ZIF268 protein-DNA complex, where the grey spheres represent zinc ions (adapted from reference 15). **B** Sample stereo view of residues interacting with base pairs (adapted from reference 17). **C** Summary of protein-DNA interactions deduced from the crystal structure (adapted from reference 15).

The crystallographic data also showed evidence of induced structural change of the DNA binding site. For instance, the major groove was found to be significantly enlarged compared to the canonical B-form and there were considerable internal variations in the geometry and orientation of the base pairs. A detailed summary of the helical parameters of the DNA binding site, when bound, is shown in Table 1.

In a second investigation, Elrod-Erickson et al. refined the structure of the same complex to a finer resolution (reference 17). Results from the previous investigation were confirmed and extended. In particular, the researchers performed circular dichroism (CD) studies and compared the CD spectrum of the ZIF268 protein-DNA complex with that of just the free DNA. As expected, the CD spectrum of the free DNA was found to be similar to that observed for canonical B-DNA. But near 275 nm, the signal increased dramatically for the ZIF268 protein-DNA complex. Because the peptide had no significant signal in this UV range, the researchers deduced that a conformational change in the DNA was the cause of the signal change, further supporting their crystallographic data.

Base pair	Displacement (Å)	Helical twist (°)	Rise (Å)	Tilt (°)	Roll (°)
2 G·C	-2.60	23.6	3.69	0.33	4.85
3 C·G	-1.91	40.5	2.91	-4.14	6.62
4 G·C	-2.20	27.3	3.40	0.74	5.08
5 T·A	-1.08	36.2	3.23	-4.49	3.45
6 G·C	-1.59	31.0	2.97	-1.66	3.48
7 G·C	-2.01	35.5	3.69	-1.45	9.23
8 G·C	-1.74	28.1	2.88	1.78	-0.96
9 C·G	-0.66	36.1	3.38	-2.61	3.21
10 G·C	-1.63	30.8	3.30	0.74	1.36
11 T·A	-0.70				
Mean	-1.61	32.1	3.27	-1.20	4.04

Table 1. Local helical parameters for the bound DNA binding site showing considerable variation from the ideal B-form DNA (adapted from reference 17).

On the computational front, much progress has been made in correctly simulating DNA in water. Due to the molecule's high charge, it has been necessary to modify approaches that have shown success with proteins. In particular, Tapia et al. performed molecular dynamics studies on the free form of the short strand of DNA used in the crystallographic studies just discussed (reference 18). The researchers used the available crystallographic data (reference 16) to seed and initiate the simulations. After a 1000ps trajectory, the DNA stabilized into a more compact canonical B-form, generally consistent with the experimental results discussed above (Figure 40).

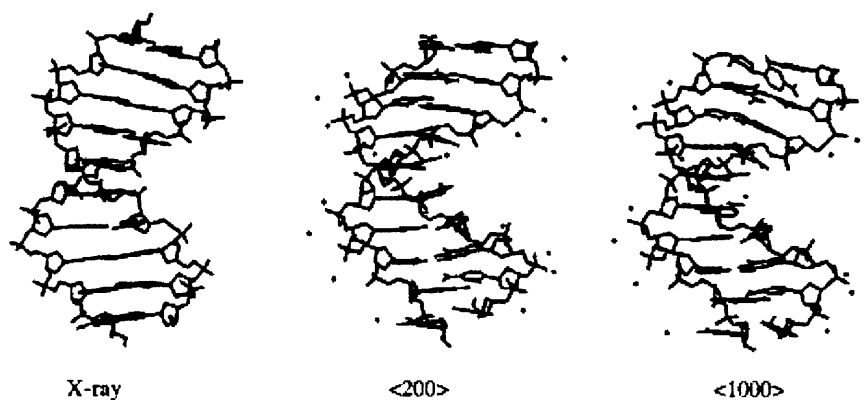X-ray   <200>   <1000>

Figure 40. 1000ps simulation trajectory initialized with the complex structure determined by x-ray crystallography (adapted from reference 18).

Following this, Roxstrom et al. published the first successful molecular dynamics simulation study on a protein-DNA system in water with fully charged phosphate groups using the ZIF268 protein-DNA complex as their model system (reference 19). The stabilized complex structure and protein-DNA interactions were found to generally agree with the experimental crystallographic data.

Based on all the work done on the ZIF268 protein-DNA system, an extensive mechanotransduction study using this system is ideal both experimentally and computationally. Although only the experimental side of this study will be discussed, computational work performed in collaboration will yield a deeper and more detailed understanding of the underlying mechanisms involved. Here, the type of mechanotransduction mechanism being considered is illustrated in Figure 41. It is well accepted that one of the methods Nature uses to regulate biochemical reactions is to induce a conformational change in the binding site of a receptor molecule such that its binding

affinity to its ligand is significantly altered. As shown schematically in Figure 41, the application of force on the receptor molecule can induce such a conformational change.

Figure 41. A simple mechanism for mechanotransduction.

In the proposed experiment, the DNA binding site of the ZIF268 protein-DNA system will be distorted with optical tweezers while ZIF268 protein binding/unbinding events will be detected using single molecule fluorescence. What can be thought of as a prelude to such a study was performed by Harada et al. in 1999 (reference 20). Here, the researchers observed interactions of single RNA polymerase molecules with a single λ-phage DNA molecule suspended in solution by two optical traps (Figure 42). They found that RNA polymerase bound nonspecifically to the DNA, diffused along the strand, but remained bound to promoter-like sites for long periods of time. When they compared binding of RNA polymerase molecules to relaxed DNA (i.e. random coils could be formed) with stretched DNA, they found that RNA polymerase dissociation rates at the promoter-like sites remained unchanged. However, there was significantly more nonspecific binding to the relaxed DNA, which the authors rationalized by the relaxed DNA's ability to wrap around RNA polymerase molecules.
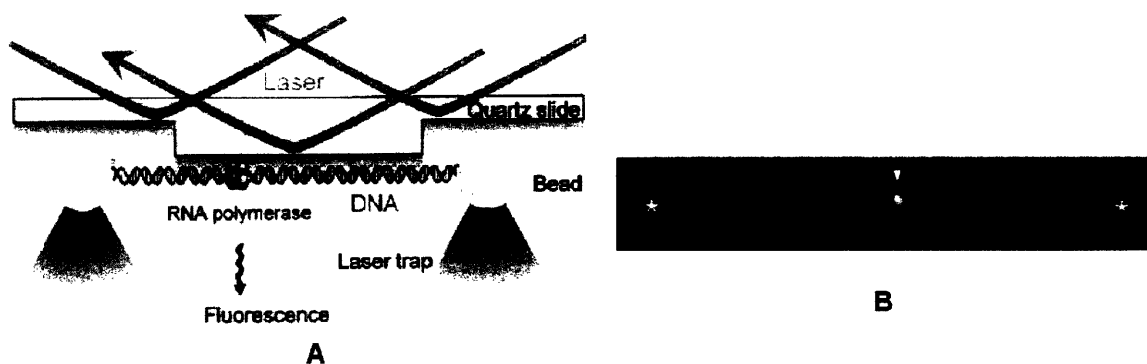

Figure 42. A Schematic diagram of experimental setup. B Image of a single fluorescently labeled RNA polymerase molecule bound to DNA (marked by arrow). The left and right stars represent the location of the two trapped beads (adapted from reference 20).

In the proposed experiment, a DNA strand containing a single ZIF268 protein binding site will be similarly stretched. Based on the structural data of the ZIF268 protein-DNA complex and previous DNA stretching studies performed both experimentally and computationally (references 21 and 22), it is believed that the binding site and its affinity to the ZIF268 protein can be significantly altered. For instance, in the simulated DNA stretching study shown in Figure 43, extensive internal structural variations were observed. The results of these simulations were consistent with results found in DNA stretching

studies using optical tweezers. More importantly, the stretched DNA structure is significantly different from the structure of the DNA binding site in the ZIF268 protein-DNA complex.
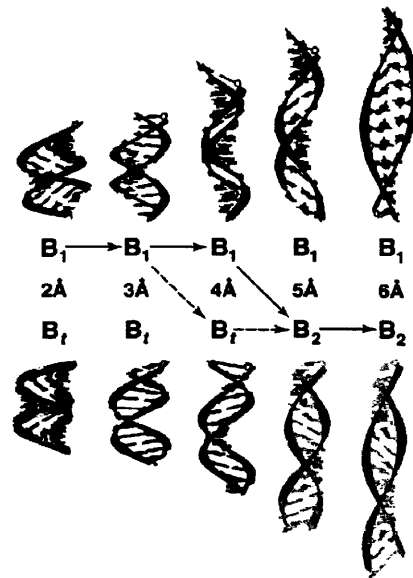

Figure 43. Ribbon representations of simulated B-DNA stretching (adapted from reference 22).

A schematic diagram of the proposed experiment is shown in Figure 44. To eliminate the possibility of nonspecific binding, the DNA binding site will be flanked by sequences known to have negligible affinity to the ZIF268 protein. In this way, this experiment proposes the first isolated mechanotransduction study at the single molecule level involving a single binding site and a single binding molecule. Assays will be adapted from the ZIF268 protein microarray study performed by Bulyk et al. (reference 23). TIRF will be used to detect the arrival of a fluorescently-labeled ZIF268 protein to the binding site. Working at relatively low concentrations of ZIF268 protein to minimize background noise, a sudden increase in photon counts by a detector such as silicon avalanche photodiode will signify a binding event. An expected time trace of photon counts is shown in Figure 45, analogous to the experimental one shown in Figure 14.
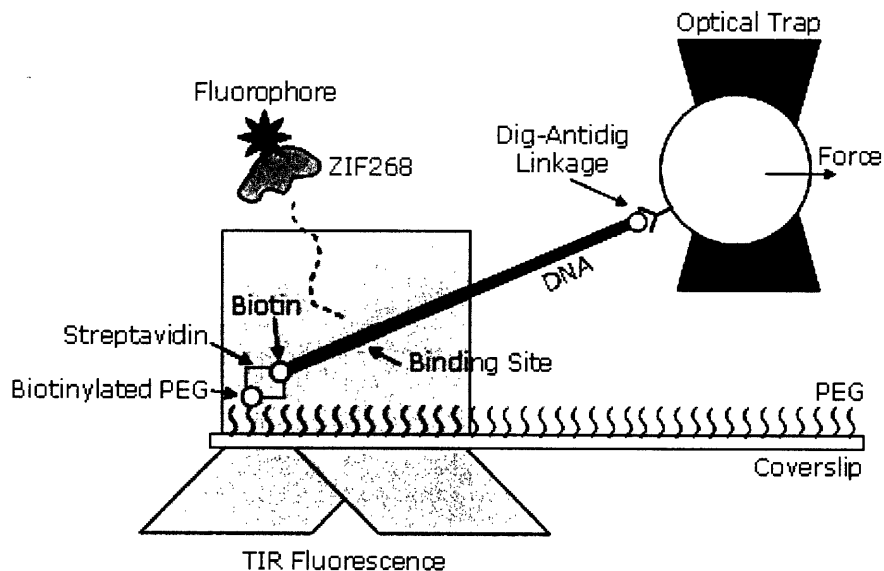

Figure 44. Schematic diagram of the proposed mechanotransduction experiment.
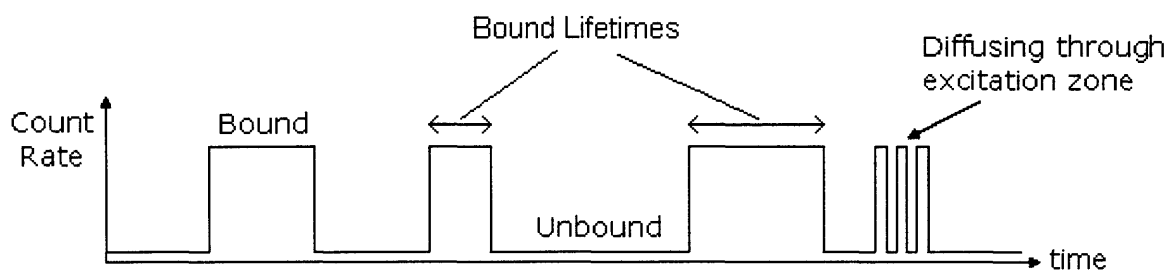
Figure 45. Expected time trace of photon counts in the proposed experiment.

A potential problem with this experimental setup is the nonspecific binding of freely diffusing ZIF268 proteins to the coverslip surface. To avoid this, the surface will be coated with polyethylene glycol (PEG), a technique used successfully in similar single molecule experiments (reference 24).

Provided that the fluorophore lifetime is sufficiently longer than the unbinding rate, a measure of the dissociation rate can be readily obtained from a long time trace of photon counts. If a statistically relevant number of bound lifetime measurements are obtained, a histogram of the number of events versus the bound lifetimes will yield an exponentially decaying distribution. Fitting an exponential function to the distribution will give a time constant, the inverse of which will be the dissociation rate. To probe mechanotransduction, these measurements will be made under the conditions of a relaxed and stretched DNA binding site. Significant differences in the dissociation rate are expected.

Due to the inability of simulating these binding/unbinding events over long periods of time, the only calculations possible for this mechanotransduction problem are the determination of the equilibrium rate constants of the ZIF268 protein-DNA system. To probe mechanotransduction, a rate constant would be determined under the conditions of a relaxed and stretched DNA binding site. Therefore, an experimental method of determining the equilibrium rate constant is needed for comparison. The proposed idea goes as follows. Consider the problem of spinning the same coin over and over again under the similar conditions. An example plot of the proportion of heads versus the number of spins is shown in Figure 46A. After a sufficiently large number of spins, a probability measure of obtaining a head on a spin can be found. Now consider a solution with a particular concentration of the ZIF268 protein surrounding the tethered DNA strand shown in Figure 44. In a similar fashion, it is expected that the fraction of time bound (i.e. formation of ZIF268 protein-DNA complex) will converge to a particular value over a long period of time. An example plot of this fraction versus time is shown in Figure 46B.
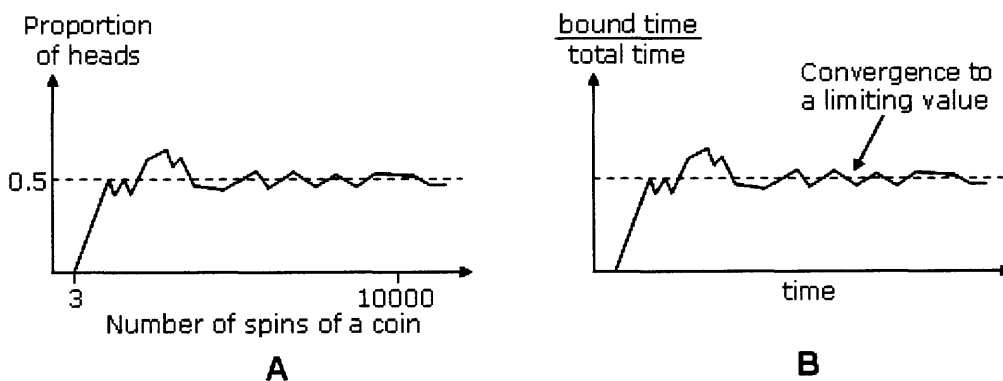

Figure 46. A Sample result of many identical spins of a coin. B Sample result from a long time trace of ZIF268 protein binding/unbinding events.

It is expected that the value of this fraction can be related to the equilibrium rate constant. To establish this relationship and to check the validity of this method, experiments must be performed at several concentrations of the ZIF268 protein. In addition, the affinity of the DNA binding site can be changed by mutating the middle three base-pair sequence. In the protein microarray work done by Bulyk et al., they found the change in binding affinity for all 64 possible mutations of the middle three base-pairs (reference 23). A sample table of their results is shown in Table 2.

Finger 2 DNA binding site	Relative signal intensity	K_d^{app}, nM
TGG	1	3.0 ± 0.57
TAG	0.751 ± 0.214	6.7 ± 1.6
GGG	0.372 ± 0.111	28
CGG	0.320 ± 0.075	35
AGG	0.256 ± 0.105	54 ± 3.3
TTG	0.153 ± 0.037	71 ± 9.8
GAG	0.150 ± 0.029	75
TCG	0.085 ± 0.025	180
CAG	0.068 ± 0.018	380 ± 67
AAA (negative control)	0.052 ± 0.015	$>5,000$

Table 2. Equilibrium rate constants found for various mutations of the middle three base-pairs of the DNA binding site in the ZIF268 protein-DNA system.

In conclusion, the experiment just proposed will yield the first direct observation of mechanotransduction at the single molecule level. Furthermore, the described experimental platform and method of analysis can be used to study other systems. Say a mutation has disabled or hindered the mechanotransduction mechanism of a complex biological system. In effect, if the mutant receptor molecule is distorted by force, no change in binding affinity results. These types of experiments would enable an isolated study of this malfunctioning mechanism. In addition, testing engineered receptors with enhanced mechanotransduction capabilities can prove to be useful clinically. Since single molecule experiments are extremely difficult to perform, coordinated efforts on the computational fronts will not only promote understanding but will aid in making these calculations a reliable and practical alternative for investigating more complex systems.

References

1. Ashkin, A., Dziedzic, J. M., Bjorkholm, J. E. & Chu, S. *Opt. Lett.* **11**(5), 288-290 (1986).

2. Svoboda, K. & Block, S. M. *Annu. Rev. Biophys. Biomol. Struct.* **23**, 247-285 (1994).

3. Neuman, K. C. & Block, S. M. *Rev. Sci. Instr.* **75**(9), 2787-2809 (2004).

4. Gittes, F. & Schmidt, C. F. *Opt. Lett.* **23**(1), 7-9 (1998).

5. Graeme, J. G. *Photodiode Amplifiers: OP AMP Solutions* (McGraw-Hill Professional, 1995).
*
6. Peterman, E. J. G., van Dijk, M. A., Kapitein, L. C. & Schmidt, C. F. *Rev. Sci. Instr.* **74**(7), 3246-3249 (2003).

7. Weiss, S. *Science* **283**, 1676-1683 (1999).

8. Ishijima, A., Kojima, H., Funatsu, T., Tokunaga, M., Higuchi, H. & Yanagida, T. *Cell* **92**, 161-171 (1998).

9. Lang, M. J., Fordyce, P. M. & Block, S. M. *Journal of Biology* **2**(1), 6.1-6.4 (2003).

10. van Dijk, M. A., Kapitein, L. C., van Mameren, J., Schmidt, C. F. & Peterman, E. J. G. *J. Phys Chem. B* **108**, 6479-6484 (2004).

11. Molloy, J. E. *Methods in Cell Biology* **55**, 205-216 (1998).

12. Wakerly, J. F. *Digital Design: Principles & Practices, 3rd Ed.* (Prentice Hall, 2001).

13. Goodman, S. D. & Nash, H. A. *Nature* **341**, 251-254 (1989).

14. Parvin, J. D., McCormick, R. J., Sharp, P. A. & Fisher, D. E. *Nature* **373**, 724-727 (1995).

15. Jamieson, A. C., Miller, J. C. & Pabo, C. O. *Nature Reviews Drug Discovery* **2**, 361-368 (2003).

16. Pavletich, N. P. & Pabo, C. O. *Science* **252**, 809-817 (1991).

17. Elrod-Erickson, M., Rould, M. A., Nekludova, L. & Pabo, C. O. *Structure* **4**, 1171-1180 (1996).

18. Tapia, O. & Velazquez, I. *J. Am. Chem. Soc.* **119**, 5934-5938 (1997).

19. Roxstrom, G., Velazquez, I., Paulino, M. & Tapia, O. *Journal of Biomolecular Structure & Dynamics* **16**, 301-312 (1998).

20. Harada, Y., Funatsu, T., Murakami, K., Nonoyama, Y., Ishihama, A. & Yanagida, T. *Biophysical Journal* **76**, 709-715 (1999).

21. Cluzel, P., Lebrun, A., Heller, C., Lavery, R., Viovy, J., Chatenay, D. & Caron, F. *Science* **271**, 792-794 (1996).

22. Kosikov, K. M., Gorin, A. A., Zhurkin, V. B. & Olson, W. K. *J. Mol. Biol.* **289**, 1301-1326 (1999).

23. Bulyk, M. L., Huang, X., Choo, Y. & Church, G. M. *PNAS* **98**, 7158-7163 (2001)

24. Rasnik, I., Myong, S., Cheng, W., Lohman, T. M. & Ha, T. *J. Mol. Biol.* **336**, 395-408 (2004)